The isolated ~680 km deep 30 May 2015 M$_W$ 7.9 Ogasawara (Bonin) Islands earthquake

Lingling Ye [a,c], Thorne Lay [a,*], Zhongwen Zhan [b,c], Hiroo Kanamori [c], Jin-Lai Hao [d]

[a] *Department of Earth and Planetary Sciences, University of California Santa Cruz, Santa Cruz, CA 95064, USA*
[b] *Scripps Institute of Oceanography, IGPP, University of California San Diego, La Jolla, CA 92093-0225, USA*
[c] *Seismological Laboratory, California Institute of Technology, Pasadena, CA 91125, USA*
[d] *Institute of Geology and Geophysics, Chinese Academy of Sciences, Beijing 100029, China*

ABSTRACT

Deep-focus earthquakes, located in very high-pressure conditions 300 to 700 km below the Earth's surface within sinking slabs of relatively cold oceanic lithosphere, are mysterious phenomena. The largest recorded deep-focus earthquake (M$_W$ 7.9) in the Izu–Bonin slab struck on 30 May 2015 beneath the Ogasawara (Bonin) Islands, isolated from prior seismicity by over 100 km in depth, and followed by only a few small aftershocks. Globally, this is the deepest (680 km centroid depth) event with M$_W \geq 7.8$ in the seismological record. Seismicity indicates along-strike contortion of the Izu–Bonin slab, with horizontal flattening near a depth of 550 km in the Izu region and rapid steepening to near-vertical toward the south above the location of the 2015 event. This event was exceptionally well-recorded by seismic stations around the world, allowing detailed constraints to be placed on the source process. Analyses of a large global data set of P, SH and pP seismic phases using short-period back-projection, subevent directivity, and broadband finite-fault inversion indicate that the mainshock ruptured a shallowly-dipping fault plane with patchy slip that spread over a distance of ~40 km with a multi-stage expansion rate (~5+ km/s down-dip initially, ~3 km/s up-dip later). During the 17 s total rupture duration the radiated energy was ~3.3×10^{16} J and the stress drop was ~38 MPa. The radiation efficiency is moderate (0.34), intermediate to that of the 1994 Bolivia and 2013 Sea of Okhotsk M$_W$ 8.3 deep earthquakes, indicating that source processes of very large deep earthquakes sample a wide range of behavior from dissipative, more viscous failure to very brittle failure. The isolated occurrence of the event, much deeper than the apparently thermally-bounded distribution of Bonin-slab seismicity above 600 km depth, suggests that localized stress concentration associated with the pronounced deformation of the Izu–Bonin slab and proximity to the 660-km phase transition likely played a dominant role in generating this major earthquake.

1. Introduction

Seismic waves radiated during rupture provide our primary information about deep earthquake processes, and detailed seismic source characterization is essential for working toward understanding the mechanism of deep events. Seismic wave radiation from deep-focus earthquakes is generally indistinguishable from that for shallow stick-slip frictional-sliding earthquakes, but the confining pressure and temperature are so high for deep-focus events that a distinct process is likely needed to account for their abrupt energy release (e.g., Green and Houston, 1995;

Houston, 2015). The two largest recorded deep-focus earthquakes both have seismic wave radiation consistent with shear dislocation on one or more fault planes, but exhibit dramatic differences in rupture characteristics. The 24 May 2013 (M$_W$ 8.3) Sea of Okhotsk earthquake near 609 km depth is the highest seismic moment, longest duration deep event (e.g., Ye et al., 2013; Wei et al., 2013; Chen et al., 2014; Zhan et al., 2014a). That rupture expanded rapidly over a 100+ km long zone, possibly involving several offset faults, at ~4.0 km/s, and the static stress drop of ~15 MPa is comparable to that for shallow intraplate events. This event had large moment-scaled radiated energy and high radiation efficiency (~0.6). In contrast, the second largest deep event is the 9 June 1994 (M$_W$ 8.3) Bolivia earthquake (e.g., Zhan et al., 2014a; Kikuchi and Kanamori, 1994; Silver et al., 1995; Kanamori et al., 1998), for which the rupture initially had rapid expansion with low energy release and then expanded slowly over about 50 km at

∼1.5 km/s, with the static stress drop being ∼114 MPa. This event had low moment-scaled radiated energy, and very low radiation efficiency (∼0.03), indicative of a very dissipative source process overall. Such profound differences in rupture behavior, comparable to the variability observed for shallow ruptures, challenge efforts to determine the fundamental nature of deep-focus earthquakes.

Currently favored ideas for nucleation and growth of deep-focus earthquakes include transformational faulting triggered by metastable olivine transforming to spinel in the cold, stressed core of the slab (e.g., Green and Burnley, 1989; Wiens et al., 1993; Green and Houston, 1995; Kirby et al., 1996; Green, 2007), thermal instability and run-away shear melting (Kanamori et al., 1998; Ogawa, 1987; Karato et al., 2001), and dehydration embrittlement (possibly involving release of H_2O or CO_2 as hydrous or carbonate phases destabilize with increasing pressure) (e.g., Silver et al., 1995; Omori et al., 2004; Meade and Jeanloz, 1991). All of these proposed mechanisms are influenced by the thermal structure of deep slabs and the deviatoric stress conditions associated with the slabs impinging on the 660-km seismic discontinuity, which resists penetration due to the associated endothermic phase change of spinel to perovskite plus ferropericlase mineralogy (Green and Houston, 1995; Karato et al., 2001).

Distinguishing between the possible mechanisms for deep-focus earthquakes is difficult because resolving their fault dimensions and source processes is very challenging. For many deep-focus events few aftershocks occur to help constrain the faulting extent and geometry (Wiens and McGuire, 1995), and the spatial extent of large deep earthquakes tends to be small and difficult to resolve by seismic waves. Various seismological methods have been applied to estimate source dimensions, rupture velocity, and source complexity for large deep events (e.g., Lundgren and Giardini, 1995; Wu and Chen, 2001; Antolik et al., 1996; Goes et al., 1997; Tibi et al., 2003a, 2003b; Kirby et al., 1995; Warren and Silver, 2006; Zhan et al., 2014b). The diversity of rupture characteristics for the two largest deep events is reinforced by observed variable processes of other large deep earthquakes (e.g., Houston, 2015). It is important to increase the observational constraints on large deep-focus earthquakes to add additional information that may help to constrain their basic mechanism.

2. The isolated 2015 deep event

The 30 May 2015 Ogasawara (Bonin) earthquake (11:23:02 UTC) has a 664 km deep hypocenter at 27.839°N, 140.493°E [USGS, National Earthquake Information Center (USGS-NEIC), http://earthquake.usgs.gov/earthquakes/eventpage/us20002ki3#scientific_origin:us_us20002ki3]. Fig. 1 shows the dramatic isolation of this deep event relative to prior seismicity in the Izu–Bonin slab. The rapid Global Centroid Moment Tensor (GCMT) point-source solution for the earthquake shown in Fig. 1 has a centroid depth of 679.9 km, with a seismic moment of 7.76×10^{20} N m (M_W 7.86). This solution has only 13% non-double couple, suggesting nearly-planar faulting, with the best double couple having nodal planes with strike 162°, dip 74°, rake −111°, and strike 37°, dip 26°, and rake −38°. Only 5 small aftershocks, the largest being an m_b 4.9 event (2 June 2015, 21:04:29 UTC, 681.4 km deep at 27.840°N, 140.616°E) close to the mainshock (depths 673.2 to 686.4 km) were located by the USGS-NEIC within a few days after the earthquake. Eight more smaller events were located nearby by the International Monitoring System as well. The earthquake also activated events throughout the Izu–Bonin slab. A shallow (9.2 km) M_W 6.2 outer rise normal faulting earthquake (Fig. 1a) occurred about 6 hours after the event (18:49:07), and four m_b 4.1 to 4.4 events occurred above the mainshock at depths of 317–417 km within 15 days of the event. Both the paucity of nearby after-

shocks and triggering of distant events in the same slab have previously been observed for some large deep earthquakes (Wiens and McGuire, 1995; Engdahl et al., 1998; Tibi et al., 2003b). The mainshock was felt widely in Japan to the north, for waves that traveled upward within the slab.

The historical catalog of deep ($\geq$ 300 km) earthquakes along the Izu–Bonin–Mariana (IBM) arc from 1900–2015 from the ISC-GEM (http://www.isc.ac.uk/iscgem; Storchak et al., 2013) and USGS-NEIC catalogs include 14 events with magnitudes $\geq$7.0. The 2015 event is much larger than the two next largest events, which have magnitudes of 7.4 at depths of 300 and 457 km. The 664 km deep hypocenter places the 2015 event much deeper than any earlier M $\geq$ 7 event along Izu–Bonin (a 559 km deep event with M_W = 7.2 struck in 1955 near 24.3°N) or the Marianas (a 595 km deep event with M_W = 7.1 struck in 1995 near 18.9°N), and more than 100 km deeper than any nearby seismicity. Of the 92 major ($M_W \geq$ 7.0) deep focus earthquakes globally recorded from 1900 to 2015, only the 19 August 2002 M_W 7.7 Tonga event has a deeper hypocentral depth (675.4 km) (USGS-NEIC).

The seismicity cross-sections in Fig. 1 indicate that the slab flattens near a depth of 550 km just 100 km north of the 2015 event, with a horizontally isolated M_W 6.7 event in 1982 having a near-vertical nodal plane that may involve tearing of the plate. The cross-section containing the 2015 event (Fig. 1c) has an almost vertical seismicity distribution, although the deep event is offset eastward from a downward projection of the seismicity trend. The seismicity is even more vertically distributed to the south, and this geometry persists into the Mariana subduction zone. Thus, the deep Ogasawara event is located in a region of strong along-strike slab distortion, but it is remarkably isolated given that its location suggests tearing, buckling or folding of the slab. Occurrence of isolated large deep earthquakes has been noted for the Izu region to the north and for other subduction zones (Lundgren and Giardini, 1994; Okino et al., 1989; Okal and Kirby, 1998; Okal, 2001; Chen and Brudzinski, 2001), indicating that localized conditions influence otherwise aseismic extensions of the slabs. The tapering-off of the main band of Benioff-zone seismicity within the Bonin slab by a depth of 550–600 km suggests a thermal constraint on the deep earthquake occurrence, but clearly the isolated 1982 and 2015 events indicate that thermal assimilation sufficient to preclude further deep earthquake occurrence after even further slab warming has not occurred. If, for example, disappearance of a central core of metastable olivine within the slab delimits the shallower earthquake activity, one would have to postulate an independent mechanism to account for the isolated deep events.

The variation in seismogenic slab penetration depth along the strike of the IBM arc system has been attributed to lateral variation in trench rollback history and subducted slab age, with larger trench retreat during the interval 30–15 Ma in the north (∼1000 km of roll-back, involving subduction of 70–95 Ma lithosphere) than in the south (∼400 km of roll-back, involving subduction of 90–115 Ma lithosphere) (Faccenna et al., 2009). This appears to have contributed to horizontal flattening of the deep Izu–Bonin slab at depths near 550 km to the north of 28°N (Lundgren and Giardini, 1994; Okal, 2001), versus the near vertical extension of the Mariana slab to depths of ∼800 km to the south of 20°N (Faccenna et al., 2009; Stern et al., 2003; van der Hilst and Seno, 1993). At present, the trench is actually advancing toward the upper Philippine Sea Plate along the entire IBM arc, with clockwise rotation of the upper plate producing back-arc extension along the Marianas. The age of subducting Pacific plate at the trench currently increases from ∼130 Ma to ∼150 Ma southward along the IBM, and recent subduction of this very old lithosphere may account for the present advance of the trench (Faccenna et al., 2009). The age of the lithosphere at the depth
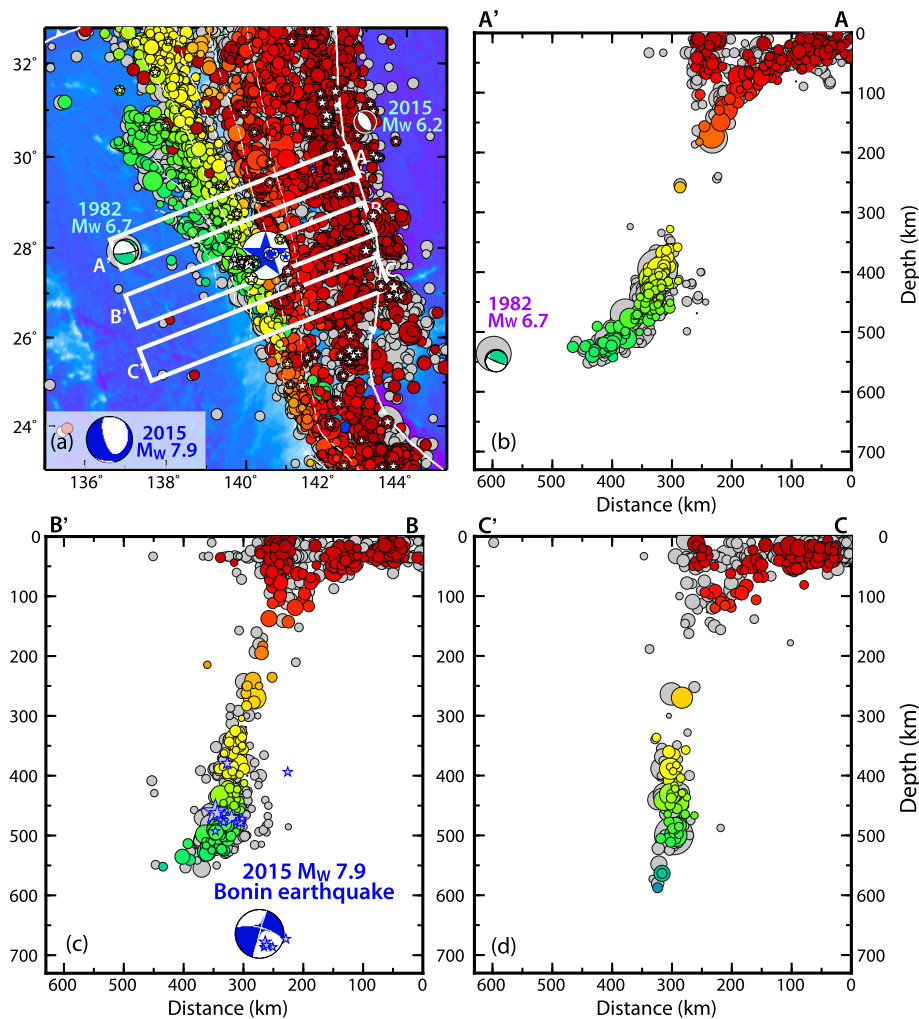
Fig. 1. The Izu–Bonin subduction zone seismicity distribution. (**a**) Map, and (**b**), (**c**) and (**d**) cross-section of earthquake locations within the westward sinking Pacific plate below the Philippine plate from catalogs of the USGS-NEIC (gray circles) and EHB (Engdahl et al., 1998) (circles color-coded by depth: reddish tones down to 200 km, yellowish from 200–400 km, greenish from 400–600 km, and blue for deeper than 600 km). The map view in (**a**) shows event epicenters including that of the 30 May 2015 event (circle with large blue star) and its gCMT focal mechanism (inset lower hemisphere projection), along with early aftershocks (depth-coded stars), the gCMT mechanism of the isolated 4 July 1982 earthquake (green focal mechanism), and locations of boxes containing the seismicity shown in cross-sections (**b**) for A′–A, (**c**) for B′–B, and (**d**) for C′–C. The focal mechanisms shown in (**b**) and (**c**) are side-view projections onto the far side of the focal sphere perpendicular to the cross-sections. The blue stars in (**c**) are early aftershocks.

of the 2015 deep event is ∼100 Ma, but lack of constraint on the distorted slab geometry near the event adds large uncertainty to this value and to any associated thermal estimate for the source environment.

3. Rupture analysis

The 2015 Ogasawara deep-focus earthquake is ideally located relative to global seismic stations, with several thousand broadband or high-quality borehole short-period instruments covering most azimuths (Fig. 2), and take-off angles ranging from almost directly upward to steeply dipping. We employed the huge data set of ground-motion recordings in a suite of analyses to determine primary features of the energy release. Unusually good resolution of the source process is achieved using the seismological observations, and this is a critical step for gaining direct insight into the basic nature of the event.
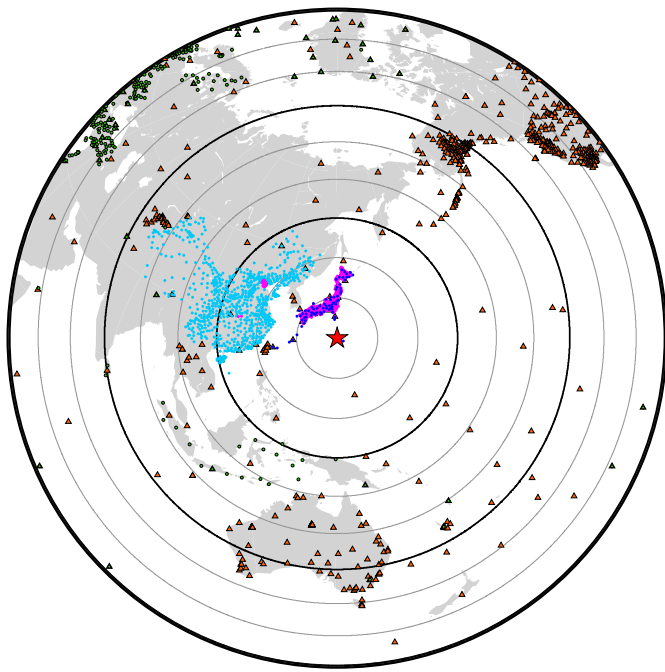
3.1. W-phase analysis

The isolated location and depth of the 2015 event in Fig. 1 is distinctive, and we confirmed the centroid depth by inverting

very long-period W-phase signals for a point-source moment tensor. This well-established procedure (Kanamori and Rivera, 2008) was applied to three-component ground displacement recordings filtered in the passband 1–5 mHz from 48 globally well-distributed stations (69–71 traces) at epicentral distances of 8 to 85°. Inversions were performed using starting depths of 650 and 720 km. Stable focal mechanisms were obtained at all depths, with optimal depths of 680.5–690.5 km, and centroid times of 5.9–9.0 s. The faulting geometry, seismic moment, and small non-double couple component are similar to the GCMT solution and are robust aspects of the rupture. When we allow for an isotropic component, we find it to be less than 1% of the moment, which is below the noise level. An average source depth near 680 km was further validated by waveform inversions of P and pP body waves and analysis of pP arrival times.
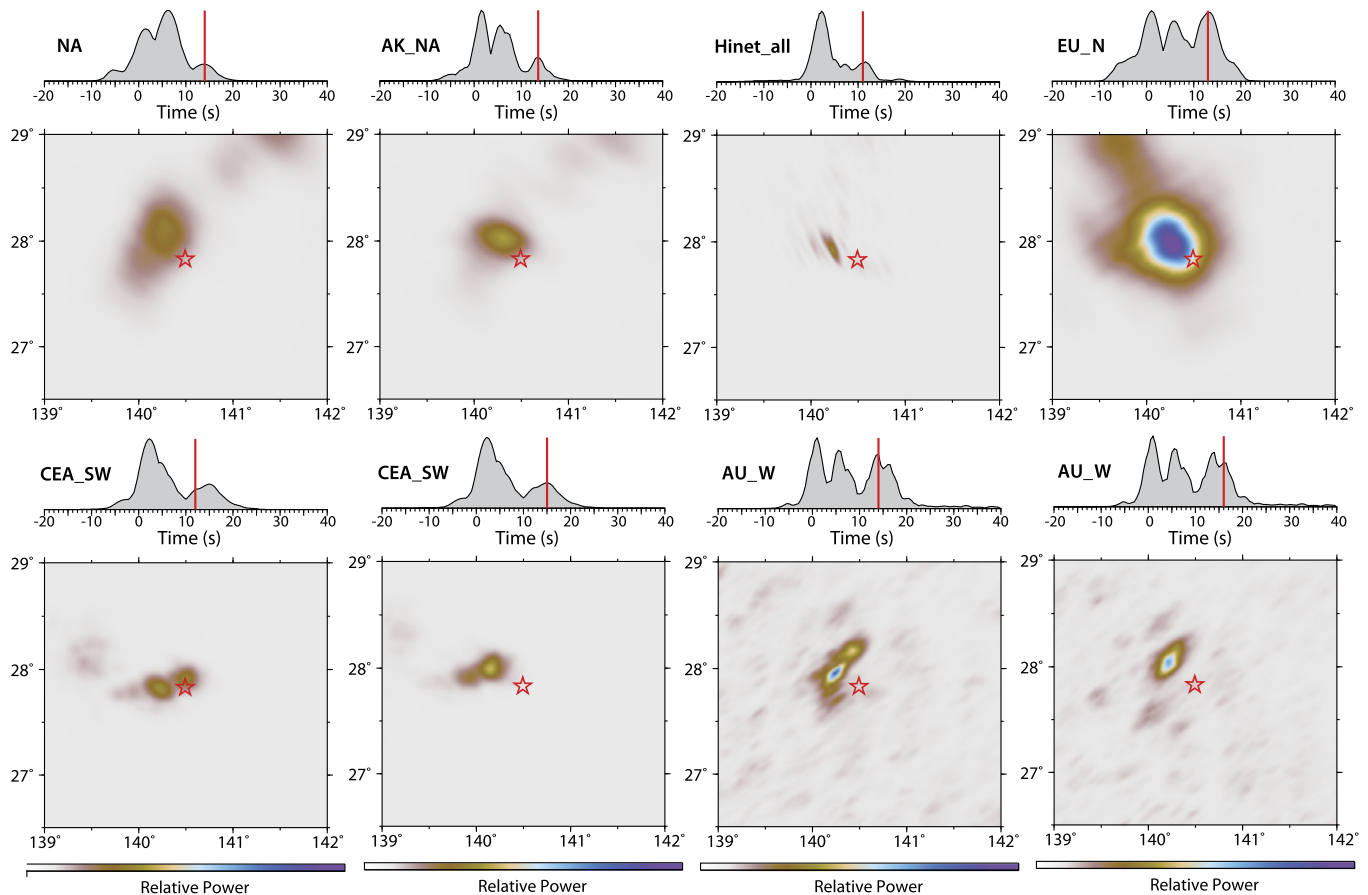
3.2. Back-projection analysis

The spatial extent and complexity of seismic energy release are the next key source attributes that can be determined by seismology, and toward this end, the superb seismic station distribution provides particular advantage. Back-projection provides a 2D time-

varying sequence of images of coherent bursts of P wave energy for a horizontal grid of subevent positions around the hypocenter without assuming a specific faulting process (Ishii et al., 2005; Xu et al., 2009; Ye et al., 2013). This procedure does not resolve differences in source depth.

We initially performed back-projections for separate large aperture regional networks in different azimuthal and distance bins, using waveform correlations to align the data for each network (Fig. S1). The Japan Hi-net borehole short-period network data were used in both 1D slant stacks and in 2D back-projections. The slant stack from northern Hi-net stations spans the largest epicentral range and indicates subevents with concentrated energy release along the NNE direction somewhat north of the hypocenter at 4.5 s and 10.5 s, and to the south at 8 s (Fig. S2). For the regional network back-projections a passband of 0.5–2.0 Hz was used in all cases other than for short-period Hi-net stations in Japan, where a 0.5–5.0 Hz passband was used. The regional network back-projections for six different networks consistently indicate three distinct intervals of coherent energy release from approximately 0–4 s, 5–10 s (Fig. S3), and 11–16 s (Fig. 3), with minor azimuthal shifts in timing indicating that the second and third intervals originate 10–20 kilometers south of the hypocenter and 25–35 km to the west/northwest, respectively (Animation S1 shows the corresponding back-projection space–time images). The apparent (horizontal) velocities of the third energy concentration in Fig. 3 range from 2.2 to 2.9 km/s. The images from the separate networks are influenced by the array response characteristics, and streaking of features along the great-circle direction to each array contaminates the source images. However, similar spatial offsets of

Fig. 2. Map displaying the locations of all stations from which seismic data were used in this study, color-coded by data source (IRIS data center, brown-triangles; Orpheus data center, green circles; China Earthquake Administration, cyan circles; NIED Hi-net, pink circles; NIED F-net, blue circles).

Fig. 3. The 0.5–2.0 Hz P wave energy near the third peak in the power distributions, 11 to 16 s after the origin time, is imaged by large-aperture networks in the conterminous U.S. and adjacent regions (NA), Alaska and North American (AK_NA), Hi-net in Japan (Hinet_all), Northern Europe (EU_N), China (CEA_SW), and Indonesia–Australia (AU_W). For the CEA_SW and AU_W projections the third peak is split and separate panels are shown for each sub-peak.
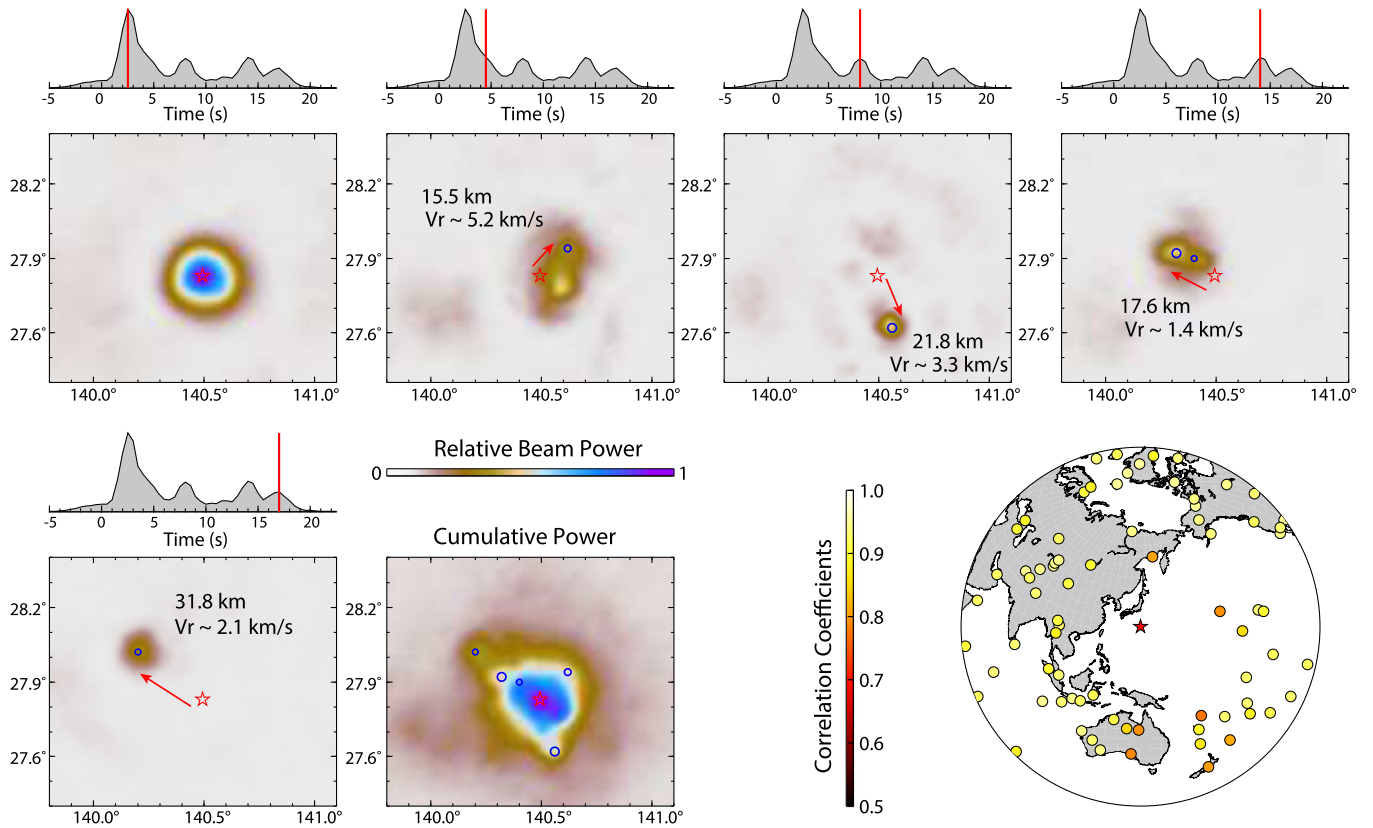
Fig. 4. The 0.1–2.0 Hz P wave energy back-projected from a global distribution of stations (the same as used later in a finite-fault inversion). The 5 snapshot panels are at 2.5 s, 4.5 s, 8 s, 14 s, and 17 s, with the power in the 4th root stack shown around the source region. The peaks that form at discrete locations (blue circles) are used to estimate the horizontal distance from the hypocenter and an apparent rupture expansion velocity from the origin, assuming a rise-time of 1.5 s. The cumulative power across the grid is shown. The global map shows the station distribution with waveform correlation indicated.

the discrete features near the same time (Fig. 3) indicate that basic features of the rupture are sensed, to varying degree, by each network.

The general consistency of the regional network back-projection images, the good signal-to-noise ratios of the data, and the absence of depth-phase interference allowed us to perform joint back-projections of short-period teleseismic P waves at all azimuths (Figs. 4, S4) to constrain the overall rupture process. This is an unstable procedure for shallow events, but works well for P waves from deep events as long as polarity reversals are corrected and efforts are made to carefully align the data onsets. The global back-projections use the same data set as used below in finite-fault inversion, with broadband signals aligned by cross-correlation and then filtered in passbands of 0.1–2.0 Hz (Fig. 4) and 0.5–2.0 Hz (Fig. S4). Fig. 4 and Animation S2 show peak bursts of energy near, east and northeast of the hypocenter in the first 5 s, 22 km to the ESE at 8 s, and from 18 to 32 km to the WNW from 14 to 17 s. The overall source dimension is ∼40 km. The global data set provides good spatial resolution of features that tend to streak along the azimuth to each array in the individual network images. We can estimate effective rupture expansion velocities from the location and timing of these image features (Fig. 4 shows values of initially 5.2 km/s toward the east and later at ∼2.1 km/s toward the west assuming horizontal rupture), but accurate rupture velocity estimation requires analysis of vertical distribution of subevents. The shear velocity near the hypocentral depth is about 5.6 km/s, so these estimates of apparent rupture expansion velocities vary from 0.93 to 0.38 times the shear velocity.

3.3. Subevent directivity analysis

Broadband P and pP waveforms at teleseismic distances are very stable, as displayed in Fig. 5. These signals are stacks in directivity bins of 0.01 s/km of varying numbers of P or pP waveforms aligned by directivity parameter, $\Gamma = p \cos(\phi_{sta} - \phi_{ref})$, where p is the ray parameter, ϕ_{sta} is the station azimuth, and the reference azimuth $\phi_{ref} = 290°$ corresponds to the average direction of the third peak in the short-period back-projections. Polarity reversals were corrected for in plotting the stacks versus directivity parameter. With the waveform stacks in Fig. 5 aligned on the first arrival, the relative move-out of two subevents about 12 s and 17 s after the first arrival can be tracked in the P waves over a wide range of azimuths (with the ∼2 s of azimuthal variation in arrival times of the arrivals being consistent with both features locating WNW from the hypocenter). Bin-average pP waveforms have generally similar total duration of motion, but the stronger attenuation of these phases (due to their extra paths up and down through the upper mantle near the source) obscures the subevents.

The move-out of secondary pulses in the waveforms was also explored using a 2D multiple sub-event procedure (Zhan et al., 2014a), applied to ground velocity recordings low-pass filtered below 0.3 Hz (Fig. 6a). These waveforms show clear move-out for azimuths of 290–300° consistent with that in Fig. 5, and can be well modeled using a 5-subevent inversion (Fig. 6c) with simple Gaussian subevent source time functions (Fig. 6d). The inversion solves for the time, wavelet duration, moment and location of each subevent, assuming a horizontal distribution. The first three subevents locate at the hypocenter, 6 km east of the hypocenter peaking at 3 s, and 6 km south of the hypocenter peaking at 6 s, with two later subevents at an azimuth of about 300° 24 km (11 s)
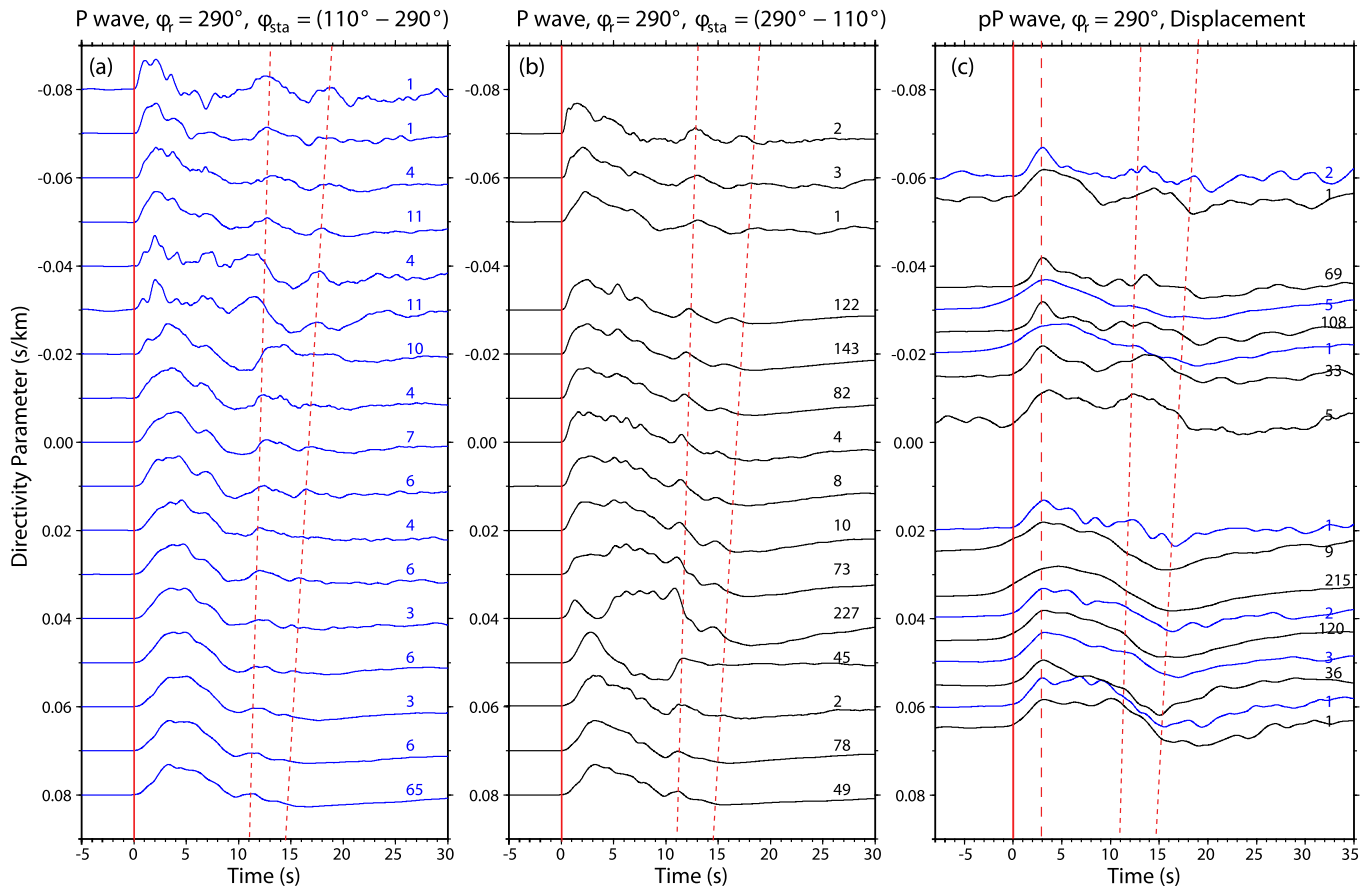
Fig. 5. Profiles of P and pP ground displacement data plotted with respect to directivity parameter relative to reference azimuth 290°, after binning and stacking the individual data in 0.01 ± 0.05 s/km intervals. The P data are plotted in the two left profiles, separating hemispheres to the NE and SW, with the two hemispheres combined in the pP profile on the right with blue indicating data from the NE hemisphere and black indicating data from the SW hemisphere. The numbers indicate how many traces are stacked in each bin. Positive directivity parameter of 0.08 s/km is in the reference azimuth direction. The data are aligned on onsets. The solid and dotted lines are at the same relative times in all panels. Narrowing of the waveforms toward positive values of directivity parameter indicates a component of rupture toward azimuth 290°. Similarity in duration of the waveforms for P and pP at a given directivity parameter requires small depth extent of the rupture, favoring the shallowly dipping nodal plane.

and 42 km (15 s) from the hypocenter. These are generally consistent with the back-projection images and with the move-out of features in the broadband displacements as seen in Fig. 6b. The overall apparent velocity to the latest subevent is about 3 km/s.

The back-projection and subevent inversion analyses do not resolve whether the subevents are on a single fault, or involve multiple faults, nor which nodal plane of the focal mechanism is involved. If we assume rupture on the steeply dipping nodal plane, the subevent ~12 s after the source and 25 km to the WNW must locate about 70 km deeper than the hypocenter. If the shallowly-dipping plane is assumed, much less vertical extent of the rupture, ~12 km, is required. Downward rupture on the steeply-dipping plane should broaden the pP depth phases relative to P, but there is no indication of this in the data profiles in Fig. 5. Comparison of up-going direct P phases to F-net stations ranging from near-vertical upward take-off angle (to station OSW at an epicentral distance of 1.7°) to horizontal take-off angles (to stations like KGM at about 11° epicentral distance) (Fig. 7a) show only about 1 s of relative move-out of the feature near 11 s, consistent with the expectations for rupture on the shallowly dipping plane, in contrast to the up to 6 s move-out among F-net stations expected for rupture on the steeply dipping plane (Fig. S5). P waves taking off at almost horizontal angles emerge near 11° epicentral distance (station KGM; Fig. 7b). Compared to steeply diving waves to more distant stations such as NIL these should have several seconds less move-out if rupture is on the steeply-dipping plane, but little move-out for the shallowly-dipping plane (Fig. S6). The P and pP waveforms in Figs. 5 and 7 sampling a very large range of take-off

angle clearly favor the shallowly dipping nodal plane, or at least a nearly horizontal distribution of subevents. In this case, the apparent rupture velocities indicated in Figs. 4 and 6 are close to actual rupture velocities, and we can use them to constrain a finite-fault inversion.

3.4. Finite-fault inversion

A single fault plane least-squares finite-source slip inversion (Harzell and Heaton, 1983; Ye et al., 2013) was performed using a well distributed teleseismic dataset of 85 P waves and 63 SH ground displacement recordings filtered in the passband 0.005–1.9 Hz for the 26° dipping nodal plane of the GCMT solution. Our approach was to impose a priori constraints on the rupture area and expansion rate based on the collective results of back-projection and subevent inversion. The fault model was parameterized with 11 subfaults along the strike direction and 14 subfaults along the dip direction (after exploring larger models), with 5 km by 5 km subfault dimensions. The subfault source time functions were parameterized by six 0.75 s rise-time triangles offset by 0.75 s time shifts, giving total possible subfault rupture durations of 5.25 s. The rupture expansion velocity was 5.0 km/s in the down-dip (eastward) direction and 3.0 km/s in the up-dip (westward) direction, guided by the back-projection images and the subevent inversion, adjusted for the 26° dip. The P wave synthetics used a $t_\alpha^* = 0.3$ s and the SH wave synthetics used a $t_\beta^* = 1.2$ s, where t^* = travel time/Q, with Q being the quality factor defined by fractional loss of energy per cycle. These values are
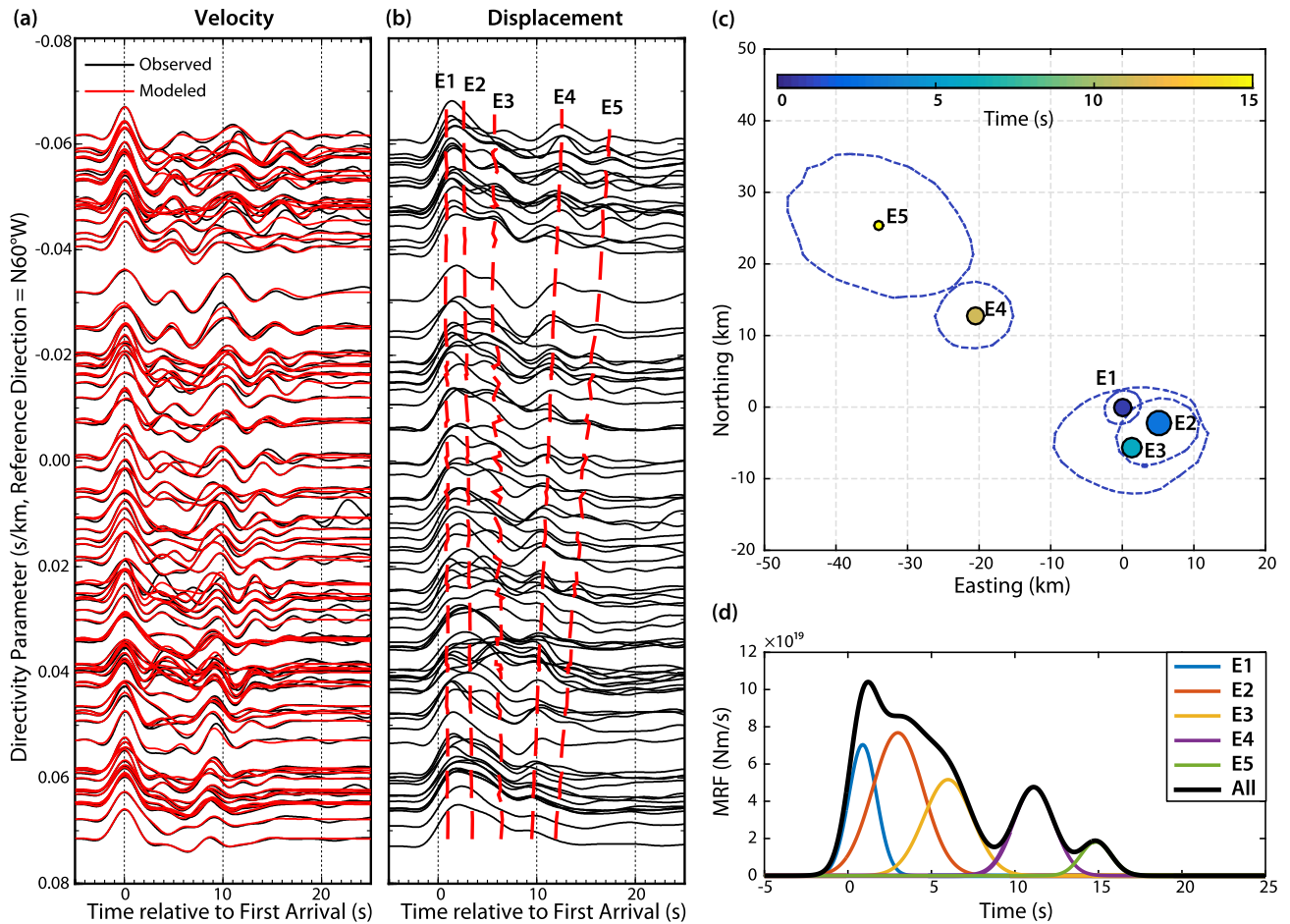
Fig. 6. (**a**) Observed, and modeled teleseismic P wave ground velocities low-pass filtered at 0.3 Hz, aligned with directivity parameters for a reference azimuth of N60°W. The traces are aligned on the first peak. (**b**) Corresponding broadband ground displacement seismograms. The synthetics in (**a**) are from a spatially distributed 5 subevent-model with relative locations shown in (**c**), with the relative timing of expected arrival peaks indicated by red dashed lines in (**b**). The blue outlines in (**c**) show uncertainty areas for each subevent. The apparent horizontal spatial dimension of the rupture is less than 45 km, but the actual fault plane is not resolved. (**d**) Plot of individual subevent source time functions (colored curves for E1 to E5) and their cumulative sum approximation of the moment rate function.
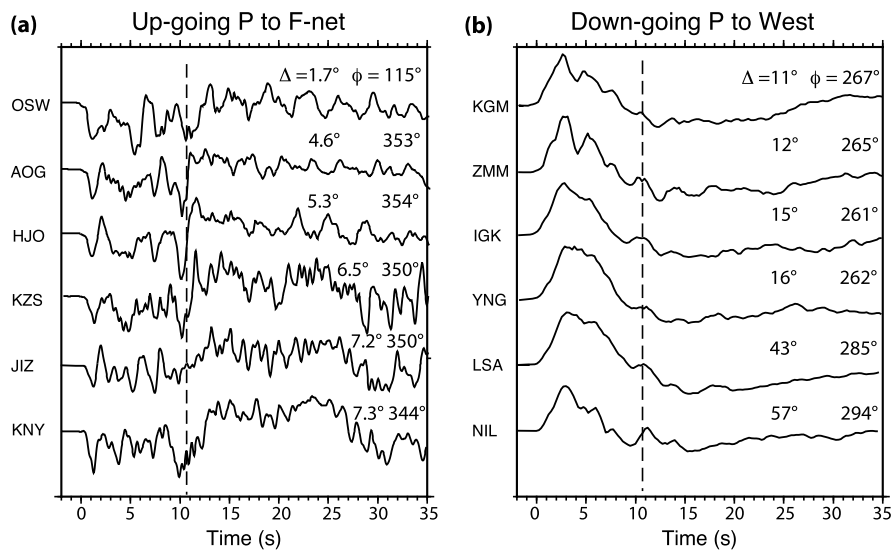
Fig. 7. Profiles of P waveforms that constrain vertical extent of the rupture. (**a**) Direct P wave ground displacements from F-net stations in Japan spanning a wide range of up-going take-off angles. (**b**) Direct P wave ground displacements at stations to the west of the source spanning take-off angles from near-horizontal at 11° to steeply down-going at teleseismic distances. In both panels the dashed line is a reference line at about the time of a subevent observed in the data in Figs. 2 and 3.
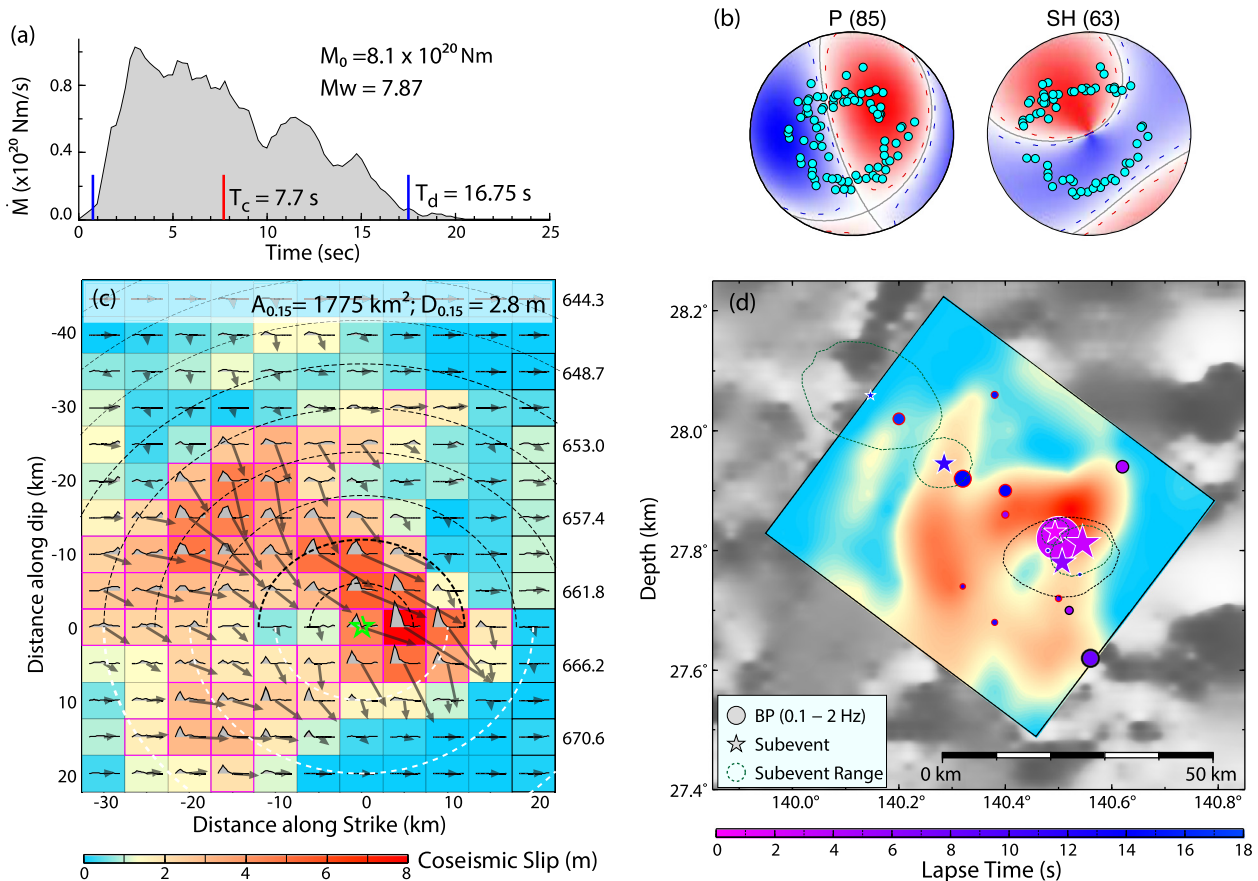
Fig. 8. Results of linear least-squares inversion for the 2015 Ogasawara earthquake slip model, for a planar fault with strike 37°, dip 26°, and hypocentral depth of 664.0 km. (**a**) The moment rate function, along with the seismic moment, corresponding M_W, centroid time (Tc; red tick) and total duration (Td; time between blue ticks). (**b**) P and SH wave lower hemisphere radiation patterns and sampling positions of the 85 P waves and 63 SH waves used in the inversion. The average rake of the solution is −37.4°. (**c**) Slip model with subfault source time functions and average slip magnitude (color scale and vector length) and direction (vector orientation in the fault-plane coordinate system). The magenta lines outline the subfaults with at least 15% of the peak-subfault moment, indicating the effective rupture area is ∼1775 km² and the average slip is ∼2.8 m over this area. The dashed circular lines indicate the rupture front in 2 s intervals. (**d**) Map view at the surface showing the spatial orientation of the smoothed slip distribution (color coded as in (**c**)) with early expansion to the east, then southeast and after 10 s toward the west and northwest. The time-coded stars, scaled by relative moment, indicate 5 subevents from the velocity waveform inversion, with dotted uncertainty areas, and the time-coded circles, scaled by relative power, are peaks from the 0.1–2.0 Hz global back-projection in Fig. 4.

average values, appropriate for a deep focus earthquake, but there are certainly path specific fluctuations in both the absolute level and frequency dependence of t^* for each observation. An empirical Green's function method can sometimes be used to account for those path properties, and Ye et al. (2013) did that for the 2013 Sea of Okhotsk earthquake, finding the values we use here.

The resulting fault-perpendicular moment rate function (Fig. 8a) has a duration of about 17 s with a total seismic moment of 8.1×10^{20} Nm (M_W 7.9); the slip distribution is shown in Fig. 8c. Peak slip is concentrated near the hypocenter, and rupture initially expands rapidly eastward to northeastward for 2 s, then southward from 4 to 5 s, followed by slower expansion to the west and northwest from 8 to 15 s. The teleseismic waveforms are well-fit by this inversion (Fig. S7), and a rather smooth slip distribution is inferred. The inversion produces subevents from spatial gradients in slip and slip velocity that have good resemblance to the discrete features imaged by back-projection and velocity waveform subevent inversion, allowing for some streaking along isochrones, but there is always a question of what parameterization is most appropriate for any earthquake rupture process (Ihmlé, 1998). We cannot preclude the presence of discrete failures (such as early triggered aftershocks) during the main rupture process. The well-resolved attributes are the ∼40 km dimension on a nearly horizontal source region, a 17 s duration with ∼8 s centroid time, concentration of

slip near the hypocenter compatible with a shear double-couple dislocation, and an $M_W = 7.9$.

3.5. Radiated energy, stress drop and radiation efficiency

The radiated energy was calculated by stacking the P wave spectra from teleseismic ground velocities for frequencies from 0.05 to 2 Hz, corrected for $t_\alpha^* = 0.3$ s. The source spectrum obtained by combining the spectrum of the moment rate function from finite-fault inversion for frequencies <0.05 Hz with the average displacement spectrum from attenuation-corrected P waves for frequencies from 0.05 to 2.0 Hz was used to apply a correction for the low-frequency radiated energy, giving a final value of 3.26×10^{16} J. The moment-scaled radiated energy is found to be 4.2×10^{-5}.

The stress drop, $\Delta\sigma$ was estimated by computing the stress at each subfault grid point for the finite-fault slip model (Fig. S8) and integrating it weighted by the slip distribution using the slip-weighted stress method (Noda et al., 2013). $\Delta\sigma$ is estimated as 38 MPa. We also trimmed the inverted finite-fault slip model to eliminate subfaults with less than 15% of the peak-subfault moment, and used the total area of significant slip and the average slip in a stress drop calculation for a circular rupture with a uniform slip, finding a value of $\Delta\sigma = 25$ MPa. We prefer the somewhat larger value from the variable slip calculation. The radiation
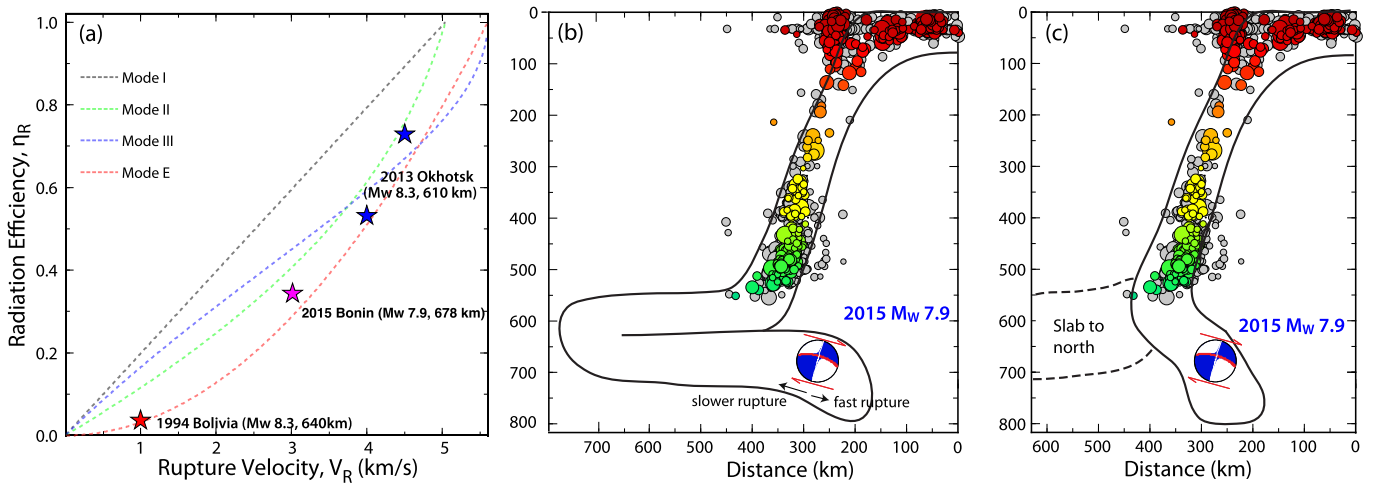
Fig. 9. (**a**) Comparison of radiation efficiency (from slip-weighted stress distributions) and rupture velocity for the 2015 Bonin deep earthquake and the 1994 Bolivia and 2013 Sea of Okhotsk earthquakes. Rupture velocities for the 1994 and 2015 events vary, but the value for the primary moment release is used in each case. Results for the 2013 Sea of Okhotsk event for rupture velocities of 4.0 and 4.5 km/s are shown. The 2015 event has intermediate efficiency relative to the 1994 Bolivia and 2013 Sea of Okhotsk events. (**b**) Interpretation of the 2015 event as locating within a folded slab continuous along strike; the seismicity from profile B′–B in Fig. 1 is shown. The rupture initially expands eastward (toward the right) at high rupture velocity of $\sim 5+$ km/s, then toward the west at slower rupture velocity of ~ 3 km/s. (**c**) Interpretation of the 2015 event as locating within a torn/buckled slab that is recumbent to the north but steeply dipping to the south. The earthquake could also be in a detached piece of slab from earlier subduction.

efficiency, $\eta_R = \frac{E_R}{\Delta W_0} = \frac{2\mu}{\Delta\sigma} \cdot \frac{E_R}{M_0} = 2 \cdot \frac{\sigma_a}{\Delta\sigma} = \sim 0.34$, where μ, σ_a, and ΔW_0 are rigidity, apparent stress, and available potential energy, respectively.

4. Discussion

The thorough seismological characterization of the 2015 Bonin earthquake slip process described above does not reveal any clear distinctions from shallow earthquakes. The measured radiation efficiency is intermediate compared with estimates for the two largest deep-focus earthquakes as shown in Fig. 9a. The radiation efficiency for the 2015 Bonin event is fairly consistent with theoretical crack models, and it is clear that large deep-focus earthquakes sample a wide range of behavior. For the 1994 Bolivia event the brittle failure component is small relative to a more ductile component, whereas for the 2013 Sea of Okhotsk, the rupture is predominantly brittle. The 2015 Bonin event is intermediate. Like the Bolivia event, it has a two-stage rupture process with initial fast down-dip rupture and relatively brittle behavior followed by slower up-dip rupture with more ductile behavior, but the average rupture expansion velocity is not as slow and the static stress drop is not as high. These large deep earthquakes have a wide range of estimated rupture velocity consistent with prior work on deep earthquakes (e.g., Houston, 2015), but there is a comparable range of rupture velocity for shallow earthquakes from supershear events to slow tsunami earthquakes or even slower rupture processes. The overall moderate energy dissipation involved in this event does not differ markedly from what is found for most shallow earthquakes. However, the lack of large aftershock activity does suggest that conditions in the source zone are distinct from those for shallower events.

The source of the 2015 Bonin event is relatively compact, spanning about 40 km in length and oblique to the trend of the shallower seismogenic slab. However, the aseismic nature of the surrounding slab makes it very difficult to evaluate whether the cold core of the slab, which could potentially host metastable olivine, is aligned with the source or not. The slab has to tear, fold or buckle to extend continuously to the position of this event (Fig. 9b, c) as also suggested by tomographic models (e.g., Wei et al., 2015), and such deformation could broaden the horizontal width of the cold region. Alternatively, there could be a chunk of detached slab (e.g.,

Chen and Brudzinski, 2001), but we believe this is unlikely given the progressive steepening of the Benioff-zone seismicity band toward the south of the Bonin slab. The principal compressional stress axis is not aligned along the down-dip extension of shallower seismicity, and is oriented dipping steeply to the northeast.

We infer that the location of the large strain release in an otherwise aseismic portion of the slab is due to stress concentration associated with strong lateral deformation of the Izu–Bonin slab and the proximity to the 660-km phase boundary. This stress concentration appears to have overcome inhibition of faulting due to progressive thermal assimilation that bounds the main Benioff-zone seismicity (Fig. 1b, c, d). Even for a buckled slab geometry such as Fig. 9c, the source region can only be warmer than the region where shallower seismicity terminates, and the lack of large local aftershocks suggests that it is difficult for even small events to occur in the source volume, and very difficult for them to grow into larger ruptures. Similar concentrated slab deformation may account for the isolated event in 1982 that lies well to the west of the flattened portion of the Izu–Bonin slab (Fig. 1b). It is not clear why the isolated mainshocks are so large; possibly there are very infrequent mineral transformation or volatile release processes that occur only under particularly high deviatoric stress conditions allowing large dynamic stress relaxations to occur.

Comparison of the average source spectra for the three deep events (Fig. 10) shows that the 1994 Bolivia event is depleted in intermediate period spectral amplitudes, reflecting the smooth, slowly rising source time function for that event, whereas the 2015 Bonin event is relatively enriched in intermediate periods due to the rapid rise time and roughness of the moment rate function. These spectra appear to reflect the relative balance of the brittle and ductile contributions to each rupture, with the 1994 Bolivia event being dominated by the smooth low rupture velocity process and the 2013 Sea of Okhotsk event being dominated by brittle high rupture velocity failure. The early, high rupture velocity stages of the 1994 and 2015 events may be associated with a distinct source process relative to the overall rupture, perhaps associated with nucleation by transformational faulting or dehydration embrittlement, followed by a more dissipative process of rupture expansion, possibly involving shear band formation or thermal runaway with melting. The occurrence of only very small aftershocks in a previously aseismic region indicates that the source volume was able to
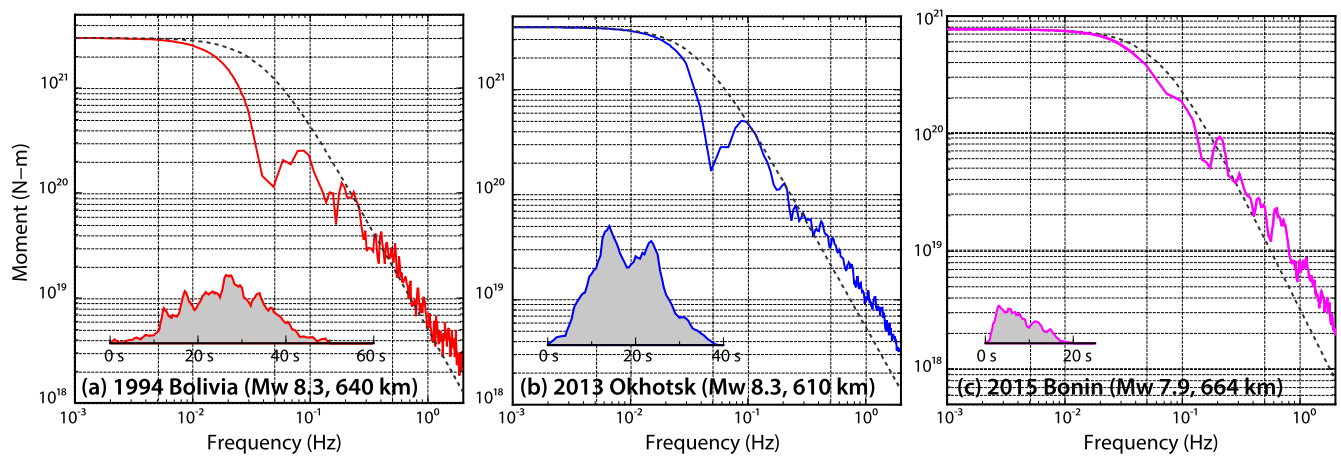
Fig. 10. Broadband source spectra obtained from finite-fault models for frequencies below 0.05 Hz and averages of teleseismic P wave spectra for higher frequencies and moment rate functions are shown for the (**a**) 1994 Bolivia, (**b**) 2013 Sea of Okhotsk, and (**c**) 2015 Bonin events. The dashed lines are reference spectra for ω-squared models with the same moment as each event, a 10 MPa stress parameter and corresponding shear wave velocity around the source. The moment rate functions are plotted on the same amplitude and time scales.

nucleate ruptures in the wake of the stress perturbation from the large event, but either limits on available strain energy or failure to achieve a threshold of slip to enable runaway rupture expansion constrained the size of the aftershocks.

5. Conclusion

The 30 May 2015 M_W 7.9 Ogasawara (Bonin) deep focus earthquake rupture began near 664 km depth, well separated from the main Bonin slab Benioff zone seismicity. The earthquake likely occurred in a buckled region of the slab, with strong contortion of the slab and resistance to penetration of the 660-km discontinuity providing high deviatoric stress concentration that overcame any thermal inhibition of faulting to produce the largest deep earthquake in the region and the deepest $M_W \geq 7.8$ earthquake yet recorded. The absence of any previous recorded seismicity in the source region and the paucity of local aftershocks for the major event indicate that earthquake nucleation in the source region is difficult. The mainshock rupture involved an initial several second long high rupture velocity brittle phase that expanded down-dip, followed by a break-out into a more dissipative process with large strain energy release with lower rupture velocity that expanded in the up-dip direction. The secondary phase was not as low velocity as for the 1994 Bolivia earthquake, and the overall radiation efficiency for the event is intermediate to that for the 1994 Bolivia and 2013 Sea of Okhotsk great deep events. The specific mechanism of the deep failure is not resolved, but it appears likely that high deviatoric stresses played a more important role than temperature in localizing the deformation.

Acknowledgements

Appendix A. Supplementary material

Supplementary material related to this article can be found online at http://dx.doi.org/10.1016/j.epsl.2015.10.049.

References

Antolik, M., Dreger, D., Romanowicz, B., 1996. Finite fault source study of the great 1994 deep Bolivia earthquake. Geophys. Res. Lett. 23, 1589–1592.

Chen, W.P., Brudzinski, M.R., 2001. Evidence for a large-scale remnant of subducted lithosphere beneath Fiji. Science 292 (5526), 2475–2479.

Chen, Y., Wen, L., Ji, C., 2014. A cascading failure during the 24 May 2013 great Okhotsk deep earthquake. J. Geophys. Res. 119, 3035–3049.

Engdahl, E.R., van der Hilst, R., Buland, R., 1998. Global teleseismic earthquake relocation with improved travel times and procedures for depth determination. Bull. Seismol. Soc. Am. 88, 722–743.

Faccenna, C., Giuseep, E.D., Funiciello, F., Lallemand, S., van Hunen, J., 2009. Control of seafloor aging on the migration of the Izu–Bonin–Mariana trench. Earth Planet. Sci. Lett. 288, 386–398.

Goes, S., Ruff, L., Winslow, N., 1997. The complex rupture process of the 1996 deep Flores, Indonesia earthquake (M_W 7.9) from teleseismic P waves. Geophys. Res. Lett. 24, 1295–1298.

Green, H.W., 2007. Shearing instabilities accompanying high-pressure phase transformations and the mechanics of deep earthquakes. Proc. Natl. Acad. Sci. USA 104, 9133–9138.

Green II, H.W., Burnley, P., 1989. A new self-organizing mechanism for deep-focus earthquakes. Nature 341, 733–737.

Green II, H.W., Houston, H., 1995. The mechanisms of deep earthquakes. Annu. Rev. Earth Planet. Sci. 23, 169–213.

Hartzell, S.H., Heaton, T.H., 1983. Inversion of strong ground motion and teleseismic waveform data for the fault rupture history of the 1979 Imperial Valley, California, earthquake. Bull. Seismol. Soc. Am. 73 (6A), 1553–1583.

Houston, H., 2015. Deep Earthquakes, Second Edition. Treatise on Geophysics, vol. 4. Elsevier, pp. 329–354.

Ihmlé, P.F., 1998. On the interpretation of subevents in teleseismic waveforms: the 1994 Bolivia deep earthquake revisited. J. Geophys. Res. 103, 17919–17932.

Ishii, M., Shearer, P.M., Houston, H., Vidale, J.E., 2005. Extent, duration and speed of the 2004 Sumatra–Andaman earthquake imaged by the Hi-Net array. Nature 435, 933–936.

Kanamori, H., Rivera, L., 2008. Source inversion of W phase: speeding up seismic tsunami warning. Geophys. J. Int. 175, 222–238.

Kanamori, H., Anderson, D.L., Heaton, T.H., 1998. Frictional melting during the rupture of the 1994 Bolivian earthquake. Science 279, 839–842.

Karato, S.-i., Riedel, M.R., Yuen, D.A., 2001. Rheological structure and deformation of subducted slabs in the mantle transition zone: implications for mantle circulation and deep earthquakes. Phys. Earth Planet. Inter. 127, 83–108.

Kikuchi, M., Kanamori, H., 1994. The mechanism of the deep Bolivia earthquake of June 9. Geophys. Res. Lett. 21, 2341–2344.

Kirby, S.H., Okal, E.A., Engdahl, E.R., 1995. The 9 June 94 Bolivian deep earthquake: an exceptional event in an extraordinary subduction zone. Geophys. Res. Lett. 22, 2233–2236.

Kirby, S.H., Stein, S., Okal, E.A., Rubie, D.C., 1996. Metastable mantle phase transformations and deep earthquake in subducting oceanic lithosphere. Rev. Geophys. 34, 261–306.

Lundgren, P., Giardini, D., 1994. Isolated deep earthquakes and the fate of subduction in the mantle. J. Geophys. Res. 99, 15,833–15,842.

Lundgren, P., Giardini, D., 1995. The June 9 Bolivia and March 9 Fiji deep earthquakes of 1994: I. Source processes. Geophys. Res. Lett. 22, 2241–2244.

Meade, C., Jeanloz, R., 1991. Deep-focus earthquakes and recycling of water into the Earth's mantle. Science 252, 68–72.

Noda, H., Lapusta, N., Kanamori, H., 2013. Comparison of average stress drop measures for ruptures with heterogeneous stress change and implications for earthquake physics. Geophys. J. Int. 193, 1691–1712.

Ogawa, M., 1987. Shear instability in a viscoelastic material as the cause of deep focus earthquakes. J. Geophys. Res. 92, 13801–13810.

Okal, E.A., 2001. "Detached" deep earthquakes: are they really? Phys. Earth Planet. Inter. 127, 109–143.

Okal, E.A., Kirby, S.H., 1998. Deep earthquakes beneath the Fiji Basin, SW Pacific: earth's most intense deep seismicity in stagnant slabs. Phys. Earth Planet. Inter. 109, 25–63.

Okino, K., Ando, M., Kaneshima, S., Hirahara, K., 1989. The horizontally lying slab. Geophys. Res. Lett. 16, 1059–1062.

Omori, S., Komabayashi, T., Maruyama, S., 2004. Dehydration and earthquakes in the subducting slab: empirical link in intermediate and deep seismic zones. Phys. Earth Planet. Inter. 146, 297–311.

Silver, P.G., Beck, S.L., Wallace, T.C., Meade, C., Myers, S.C., James, D.E., Kuehnel, R., 1995. Rupture characteristics of the deep Bolivian earthquake of 9 June 1994 and the mechanism of deep-focus earthquakes. Science 268, 69–73.

Stern, R.J., Fouch, M.H., Klemperer, S.L., 2003. An overview of the Izu–Bonin–Mariana Subduction factory. In: Inside the Subduction Factory. In: Geophysical Monograph, vol. 138. American Geophysical Union, pp. 175–222.

Storchak, D.A., Di Giacomo, D., Bondár, I., Engdahl, E.R., Harris, J., Lee, W.H.K., Villaseñor, A., Bormann, P., 2013. Public release of the ISC-GEM global instrumental earthquake catalogue (1900–2009). Seismol. Res. Lett. 84 (5), 810–815.

Tibi, R., Bock, G., Wiens, D.A., 2003a. Source characteristics of large deep earthquakes: constraint on the faulting mechanism at great depths. J. Geophys. Res. 108 (B2), 2091. http://dx.doi.org/10.1029/2002JB001948.

Tibi, R., Wiens, D.A., Inoue, H., 2003b. Remote triggering of deep earthquakes in the 2002 Tonga sequences. Nature 424, 921–925.

van der Hilst, R., Seno, T., 1993. Effects of relative plate motion on the deep structure and penetration depth of slabs below the Izu–Bonin and Mariana island arcs. Earth Planet. Sci. Lett. 120, 395–407.

Warren, L.M., Silver, P.G., 2006. Measurement of differential rupture durations as constraints on the source finiteness of deep-focus earthquakes. J. Geophys. Res. 111, B06304.

Wei, S., Helmberger, D., Zhan, Z., Graves, R., 2013. Rupture complexity of the M_W 8.3 sea of Okhotsk earthquake: rapid triggering of complementary earthquakes? Geophys. Res. Lett. 40, 5034–5039.

Wei, W., Zhao, D., Xu, J., Wei, F., Liu, G., 2015. P and S wave tomography and anisotropy in Northwest Pacific and East Asia: constraints on stagnant slab and intraplate volcanism. J. Geophys. Res. 120, 1642–1666.

Wiens, D.A., McGuire, J.J., 1995. The 1994 Bolivia and Tonga events: fundamentally different types of deep earthquakes? Geophys. Res. Lett. 22, 2245–2248.

Wiens, D.A., McGuire, J.J., Shore, P.J., 1993. Evidence for transformational faulting from a deep double seismic zone in Tonga. Nature 364, 790–793.

Wu, L.-R., Chen, W.-P., 2001. Rupture of the large (M_W 7.8), deep earthquake of 1973 beneath the Japan sea with implications for seismogenesis. Bull. Seismol. Soc. Am. 91, 102–111.

Xu, Y., Koper, K.D., Sufri, O., Zhu, L., Hutko, A.R., 2009. Rupture imaging of the M_W 7.9 12 May 2008 Wenchuan earthquake from back projection of teleseismic P waves. Geochem. Geophys. Geosyst. 10, Q04006. http://dx.doi.org/10.1029/2008GC002335.

Ye, L., Lay, T., Kanamori, H., Koper, K.D., 2013. Energy release of the 2013 M_W 8.3 Sea of Okhotsk earthquake and deep slab stress heterogeneity. Science 341, 1380–1384.

Zhan, Z., Kanamori, H., Tsai, V.C., Helmberger, D.V., Wei, S., 2014a. Rupture complexity of the 1994 Bolivia and 2013 Sea of Okhotsk deep earthquakes. Earth Planet. Sci. Lett. 285, 89–96.

Zhan, Z., Helmberger, D.V., Kanamori, H., Shearer, P.M., 2014b. Supershear rupture in a M_W 6.7 aftershock of the 2013 Sea of Ohotsk earthquake. Science 345, 204–206.

Supplementary Materials

The isolated 680 km deep 30 May 2015 M~W~ 7.9 Ogasawara (Bonin) Islands earthquake

Lingling Ye[1,3], Thorne Lay[1,*], Zhongwen Zhan[2,3], Hiroo Kanamori[3], Jin-Lai Hao[4]

[1]Department of Earth and Planetary Sciences, University of California Santa Cruz, Santa Cruz, CA 95064, USA.
[2]Scripps Institute of Oceanography, IGPP, University of California San Diego, La Jolla, 92093-0225CA
[3]Seismological Laboratory, California Institute of Technology, Pasadena, CA 91125 USA.
[4]Institute of Geology and Geophysics, Chinese Academy of Sciences, Beijing, 100029, China.
*Corresponding author: Thorne Lay (tlay@ucsc.edu; 831-459-3164)

Supplementary Figs. S1-S8
Animations S1-S2
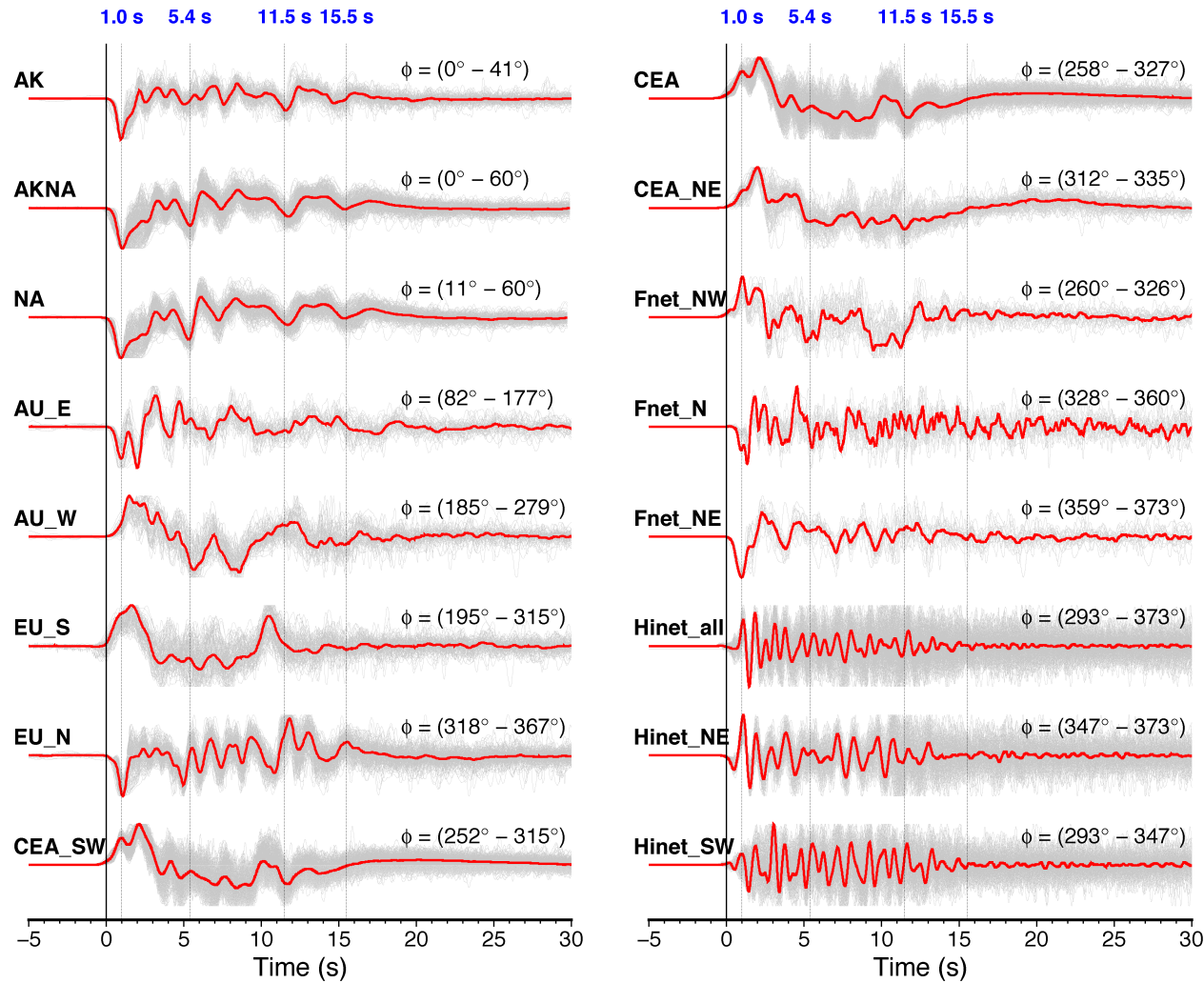
Fig. S1. Amplitude-normalized, first-arrival-aligned P waveforms for large-aperture networks at various azimuths from the source (gray traces) and their linear average (red traces). Instrument responses have not been removed. Bandpass filtered versions of these aligned waveforms are used in back-projection imaging for each network separately. A first-motion polarity reversal across the Hi-net stations in Japan was corrected for in joint back-projection of all Hi-net stations.

2
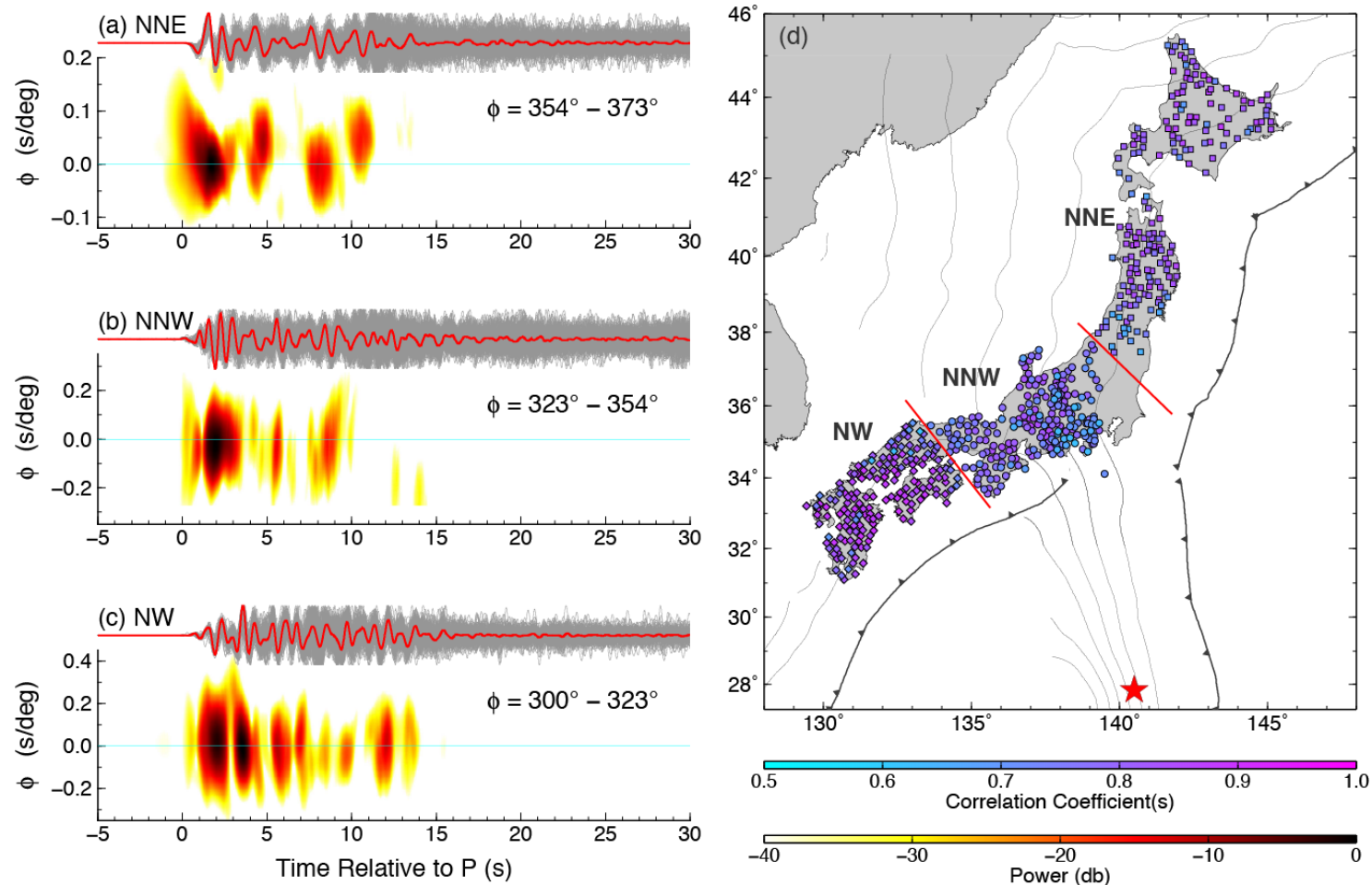
Fig. S2. One-dimensional slant-stacks of the short-period Hi-net data in azimuthal bins of (**a**) 354-373°, (**b**) 323-354°, and (**c**) 300-323°. The data are aligned on the P arrivals, and slowness differences are given with respect to the first arrival. The waveforms in each sector are normalized and superimposed (gray traces), along with the linear average (red trace: zero relative slowness stack). The power in the stacks for varying relative slowness is color-contoured. (**d**) shows the groups of stations used in each slant-stack with the correlation coefficient relative to the mean trace color-coded. The red star is the epicentral location of the 2015 event. Positive relative slowness indicates rupture closer to the stations; the lack of strong shifts in slowness throughout the 15 s of significant power indicates a spatially concentrated source.

3
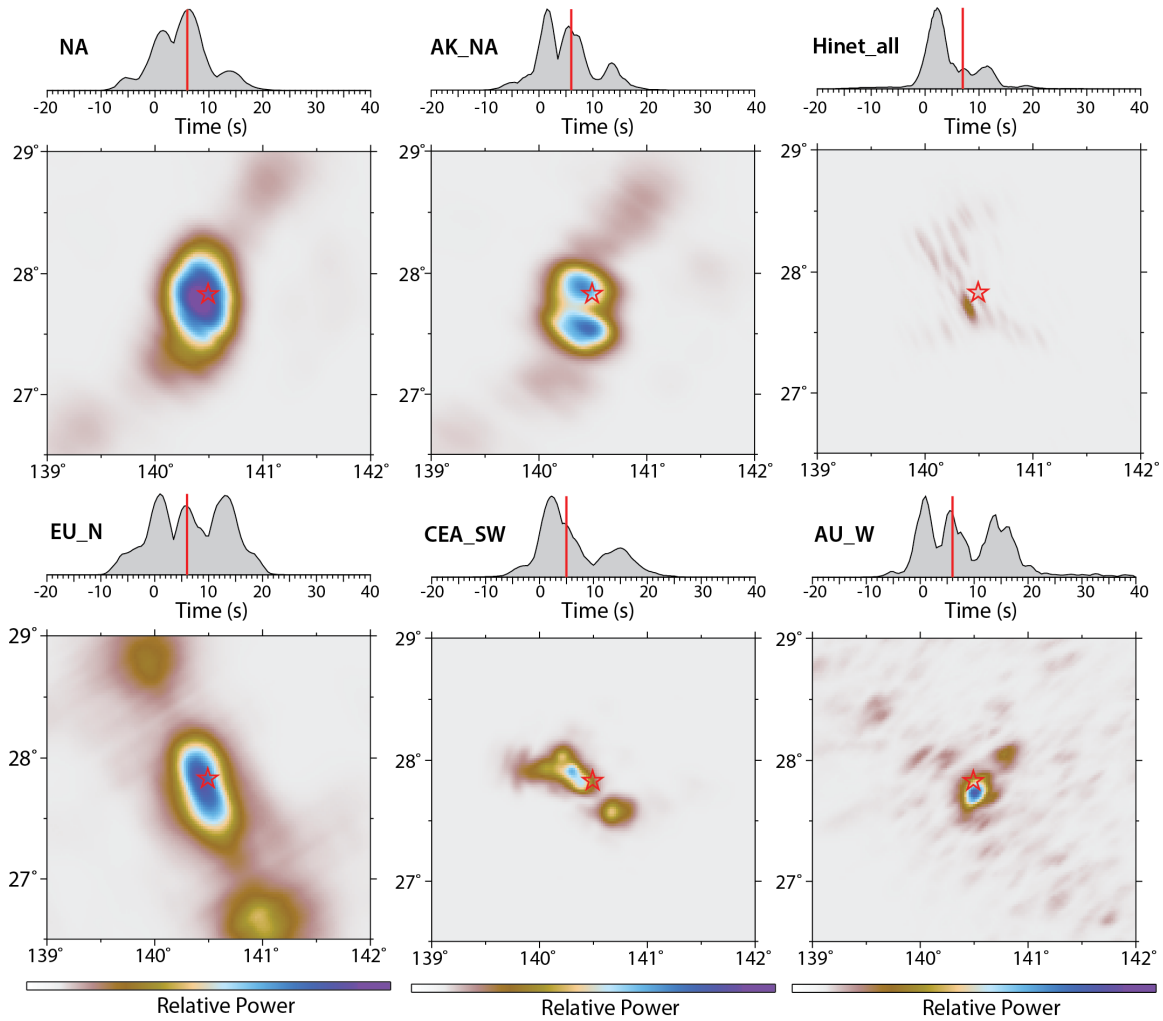
Fig. S3. Snapshots from back-projection images (4th root stacks) for signal near the second peak, 5 to 7 s after the origin time from large-aperture networks in the conterminous U.S. and adjacent regions (NA), Alaska and North American (AK_NA), Hi-net in Japan (Hinet_all), Northern Europe (EU_N), China (CEA_SW), and Indonesia-Australia (AU_W).

4
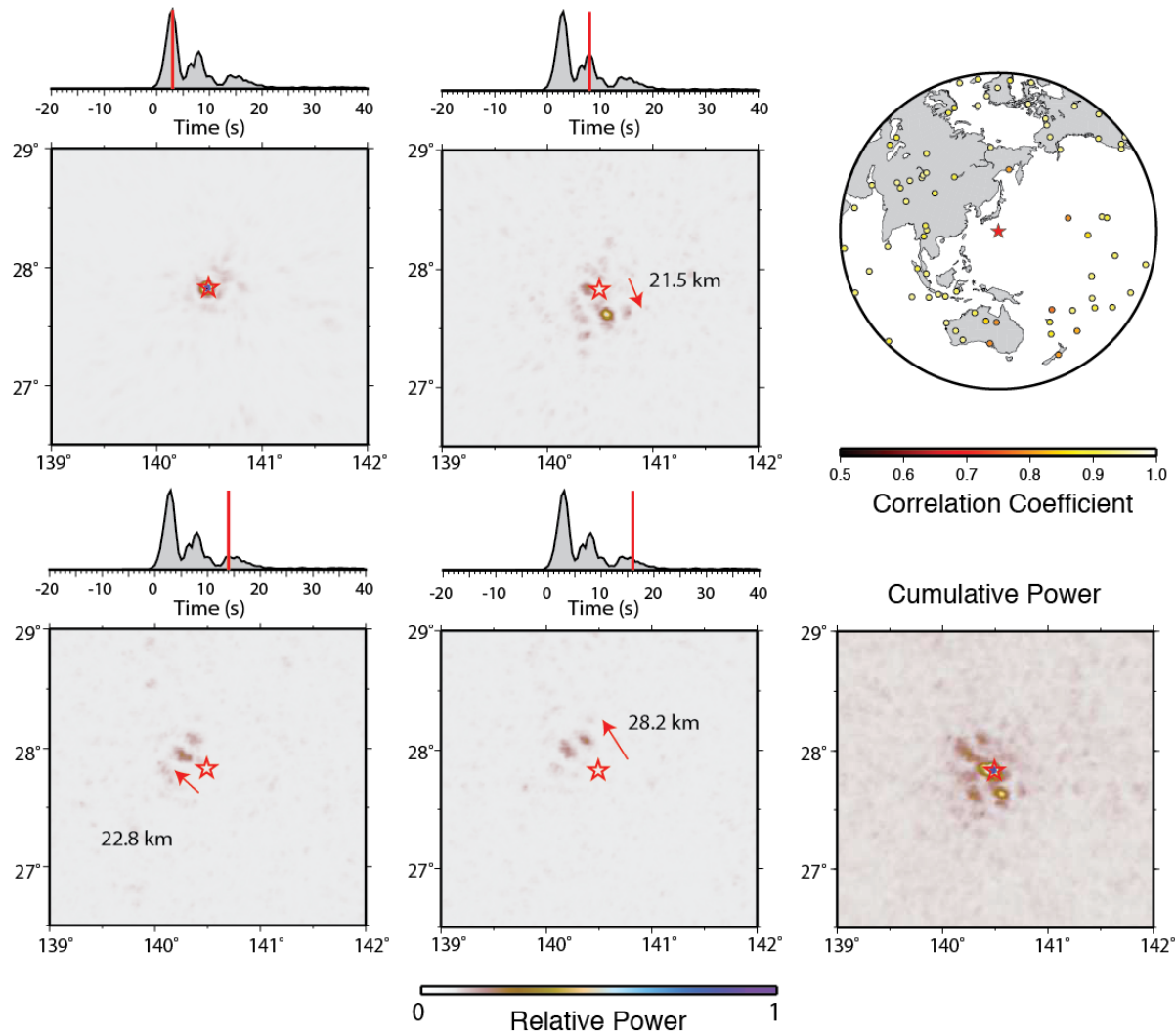
Fig. S4. The 0.5-2.0 Hz P wave energy back-projected from a global distribution of stations (the same as used later in a finite-fault inversion). The four panels on the left and center are snapshots at 3 s, 8 s, 14 s, and 16 s, with the power in the 4th root stack shown around the source region. The peaks that form at discrete locations are used to estimate the horizontal distance from the hypocenter and an apparent rupture expansion velocity from the origin. The global map shows the station distribution. The cumulative power of the images integrated over time is shown on the lower right, indicating a total source dimension of about 40 km, slightly elongated to the south and northwest.
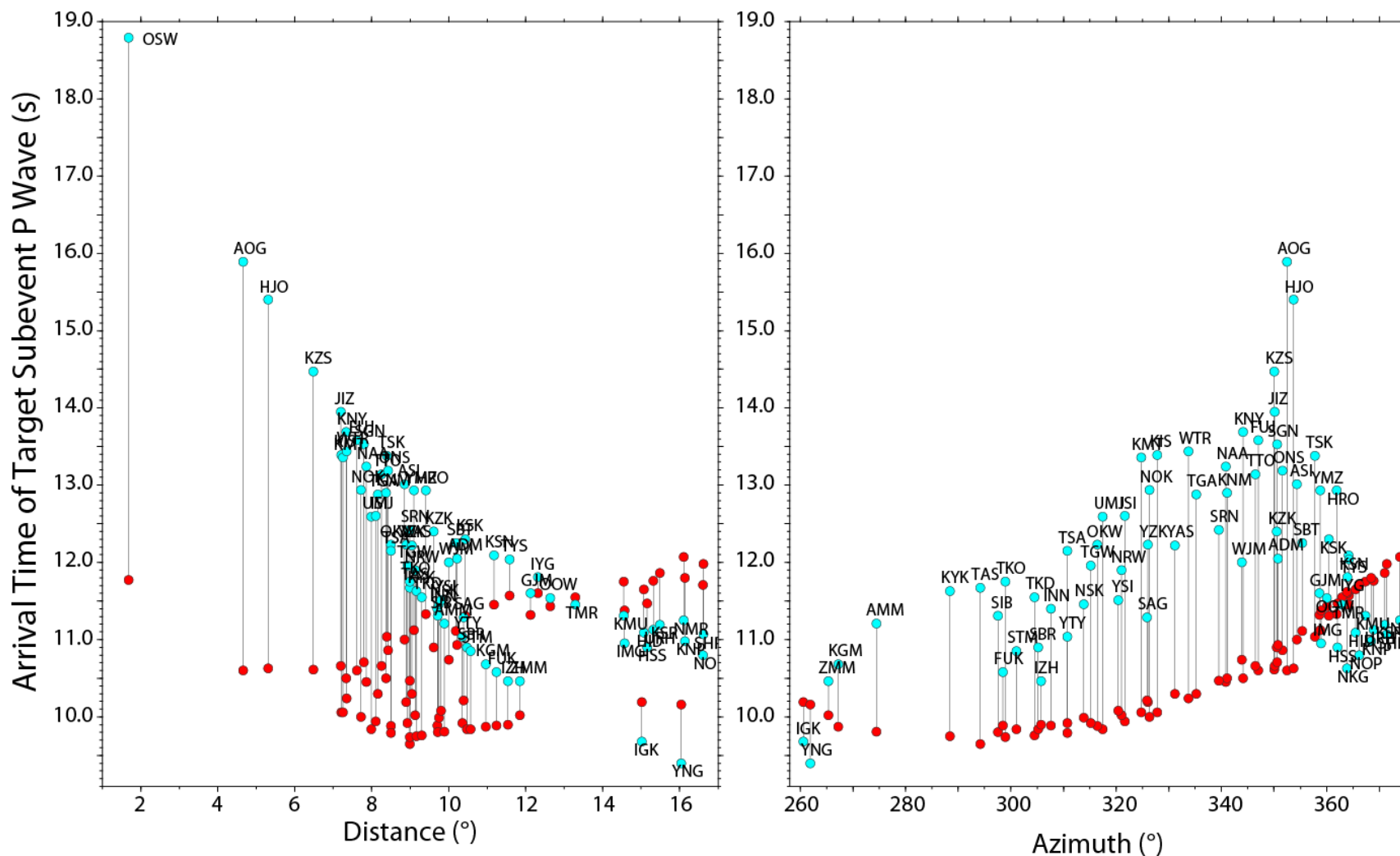
Fig. S5. Calculated time differences from the origin to the target third peak 25 km toward the NNW (described in the text) for travel time model IASP91 for up-going p phases (epicentral distances less than 11°) or down-going P phases (epicentral distances greater than 11°) to F-net stations, assuming the target subevent is on either the steeply-dipping (cyan) or the shallowly-dipping (red) dipping fault plane choice at depths of 748 km and 666 km, respectively. Note that much larger time variations due to azimuth and take-off angle variations are expected for the steeply-dipping fault plane.
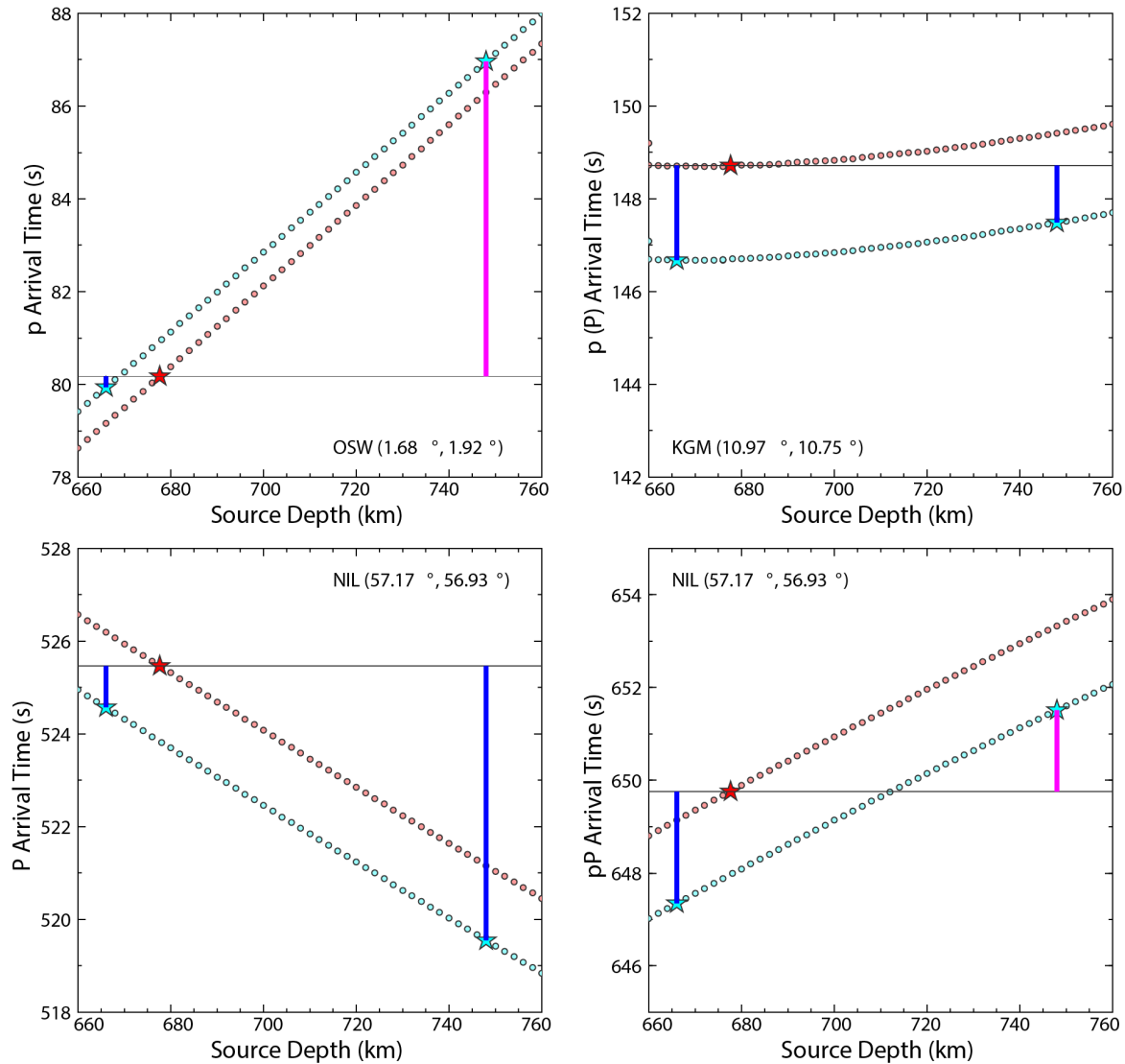
Fig. S6. Calculated travel times (IASP91 model) for arrivals of up-going p, and teleseismic P and pP phases at stations OSW, KGM and NIL versus source depth. The hypocenter is indicated by the red star. Target subevent positions 25 km to the NNW projected to the shallowly dipping fault plant (source depth 666 km) and the steeply dipping fault plane (source depth 748 km) and corresponding distance (second distance in name label) to each station are shown by the cyan stars. Blue lines indicates how much time has to be added to the absolute time shift of the subevent (12 s) to calculate the relative arrival time, pink lines indicate how much time has to be subtracted from the absolute time shift of the subevent to calculate the time relative to the first arrival.

7
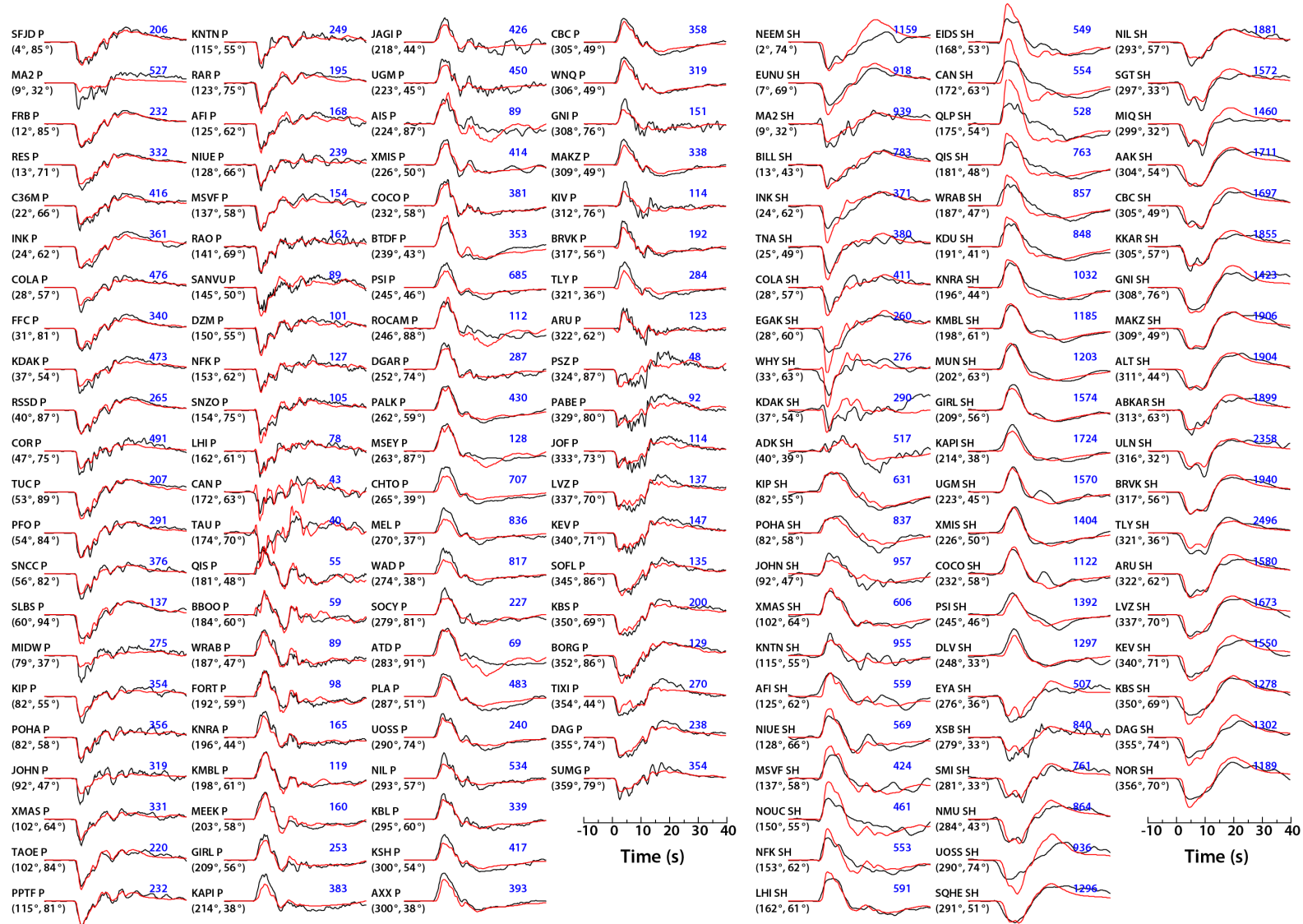
Fig. S7. Observed (black lines) and modeled (red lines) P and SH waveforms for the 2015 Bonin earthquake. The synthetic waveforms are for the finite-fault model in Fig. 8. The peak-to-peak amplitudes in microns are shown by each trace; waveform mismatches for very low amplitude signals indicate that they are near radiation nodes.

8
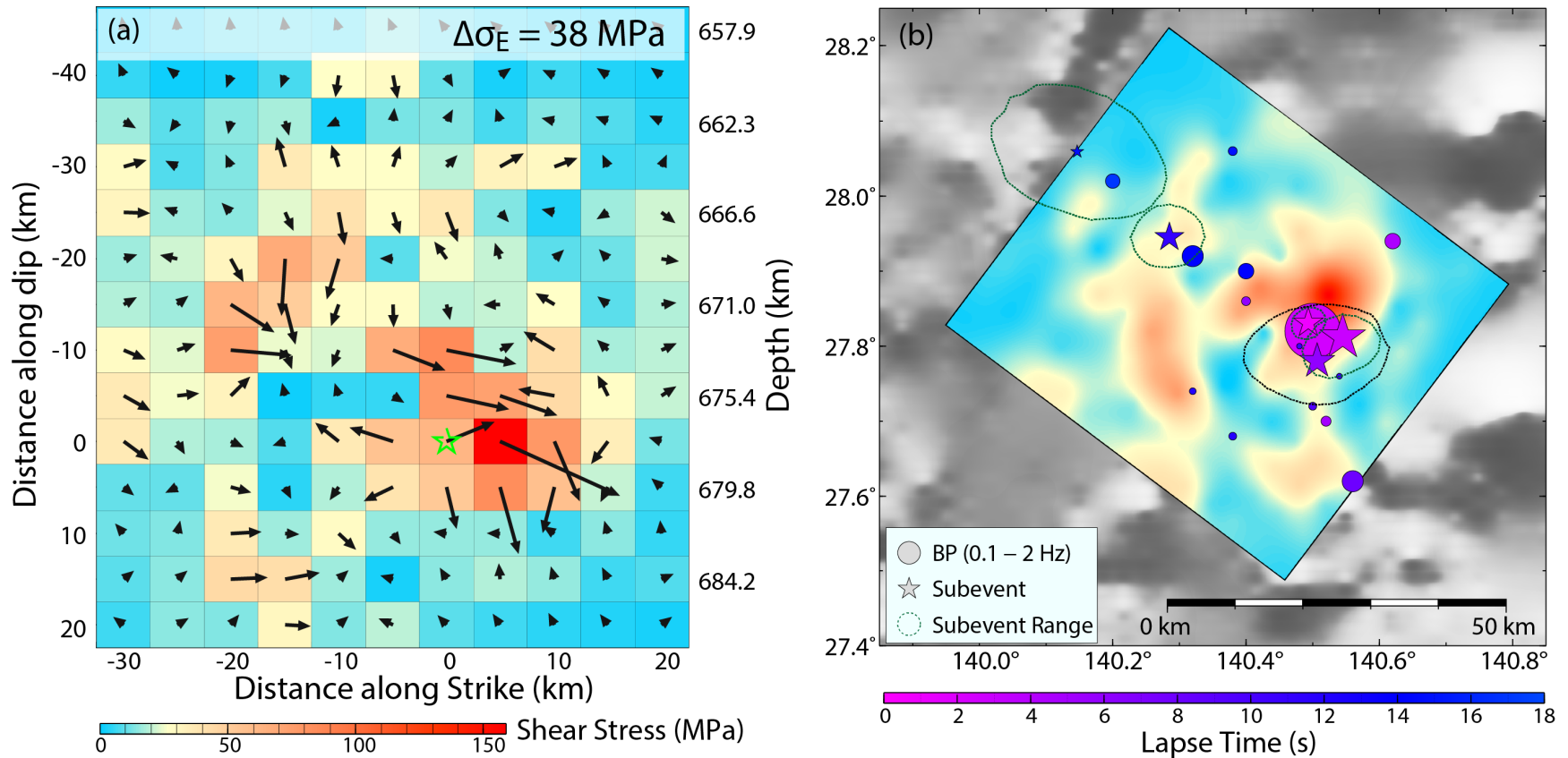
Fig. S8. (a) Average shear stress drop $\Delta\sigma_E$ which is the average stress drop weighted by the average slip defined by Noda et al. (2013). The magnitude of $\Delta\sigma_E$ is given by the color code. The arrows give the magnitude and the direction $\Delta\sigma_E$ at the center of each sub-fault for the finite-fault model shown in Fig. 8. The estimated static stress drop for this rupture model is 38 MPa. (b) Map view at the surface showing the stress variation on the fault model (colors are relative to the shear stress scale in (a)), relative to results of ground velocity subevent inversion and back-projection. The time-coded stars, scaled by relative moment, indicate 5 subevents from the velocity waveform inversion, with dotted uncertainty areas, and the time-coded circles, scaled by relative power, are peaks from the 0.1-2.0 Hz global back-projection in Fig. 3.